Multiwavelength, aerosol lidars at Maïdo supersite, Reunion Island, France: instruments description, data processing chain and quality assessment

Dominique Gantois[1], Guillaume Payen[2], Michaël Sicard[1], Valentin Duflot[1,3], Nelson Bègue[1], Nicolas Marquestaut[2], Thierry Portafaix[1], Sophie Godin-Beekmann[4], Patrick Hernandez[2], Eric Golubic[2].

[1] LACy, Laboratoire de l'Atmosphère et des Cyclones (UMR 8105 CNRS, Université de La Réunion, Météo-France), Saint-Denis de La Réunion, France
[2] Observatoire des Sciences de l'Univers de La Réunion (OSU-Réunion), UAR3365, Université de La Réunion, CNRS, IRD, Météo-France, 97490 Saint-Denis de La Réunion, France
[3] now at: Department for Atmospheric and Climate Research, NILU – Norwegian Institute for Air Research, Kjeller, Norway
[4] LATMOS, Laboratoire Atmosphères, Observations Spatiales, UPMC, Paris, France

Correspondence to : Dominique Gantois (Dominique.gantois@univ-reunion.fr)

Abstract. Understanding optical and radiative properties of aerosols and clouds is critical to reduce uncertainties in climate models. For over 10 years, the Observatory of Atmospheric Physics of La Réunion (OPAR, 21.079°S, 55.383°E) has been operating three active lidar instruments (named Li1200, LiO3S and LiO3T) providing time-series of vertical profiles from 3 to 45 km of the aerosol extinction and backscatter coefficients at 355 and 532 nm, as well as the linear depolarization ratio at 532 nm. This work provides a full technical description of the three systems, details about the methods chosen for the signal preprocessing and processing, and an uncertainty analysis. About 1737 night-time averaged profiles were manually screened to provide cloud-free and artifact-free profiles. Data processing consisted in Klett inversion to retrieve aerosol optical products from preprocessed files. The measurement frequency was lower during the wet season and the holiday periods. There is a good correlation between the Li1200 and LiO3S in terms of stratospheric Aerosol Optical Depth (AOD) at 355 nm (0.001-0.107; R = 0.92 ± 0.01), and with the LiO3T in terms of Angström exponent 355/532 (0.079-1.288; R = 0.90 ± 0.13). The lowest values of the averaged uncertainty of the aerosol backscatter coefficient for the three time-series are 64.4 ± 31.6 % for the LiO3S, 50.3 ± 29.0 % for the Li1200, and 69.1 ± 42.7 % for the LiO3T. These relative uncertainties are high for the three instruments because of the very low values of extinction and backscatter coefficients for background aerosols above Maïdo observatory. Uncertainty increases due to Signal to Noise Ratio (SNR) decrease above 25 km for the LIO3S and Li1200, and 20 km for the LiO3T. The Lidar Ratio (LR) is responsible for an uncertainty increase below 18 km (10 km) for the LiO3S and Li1200 (LiO3T). The LiO3S is the most stable instrument at 355 nm due to less technical modifications and less misalignments. The Li1200 is a valuable addition to fill in the gaps in the LiO3S time-series at 355 nm or for specific case-studies about the middle and low troposphere. Data described in this work are available at https://doi.org/10.26171/rwcm-q370 (Gantois et al., 2024).

1. Introduction

46 Uncertainties concerning aerosol and cloud optical and radiative properties strongly affect surface climate and
47 also the accuracy in climate models (Hansen et al., 1997; Alexander et al., 2013). Aerosols can be of multiple
48 origins, compositions, sizes, and shapes, but can also interact at different temporal and spatial scales and be
49 influenced by various dynamical processes. This makes their observation at the global scale and the modelling of
50 their properties challenging. Improving our knowledge in this area implies to use different measurement techniques
51 (in situ, active and passive remote sensing methods) synergistically and to provide continuous timeseries of high-
52 resolution measurements in the low and middle atmosphere.

53 The Observatory of Atmospheric Physics of La Réunion (OPAR), located on Réunion Island near Madagascar,
54 is currently equipped with more than 50 instruments distributed over three different sites: two historical coastal
55 sites in the north, and a high-altitude site (Maïdo observatory, 2160 m asl, Baray et al., 2013), which now houses
56 more than two-thirds of these instruments. OPAR is part of many international networks, including GAW (Global
57 Atmospheric Watch), NDACC (Network for the Detection of Atmospheric Composition Change), SHADOZ
58 (Southern Hemisphere Additional OZonesondes), and AERONET (Aerosol Robotic Network). Additionally, it is
59 a part of the European research infrastructures ACTRIS (Aerosol, Clouds, and Trace Gases Research
60 Infrastructure) and ICOS (Integrated Carbon Observing System).

61 Maïdo observatory (21.079°S, 55.383°E) is one of the very few active observational sites in the Southern
62 Hemisphere (SH). It is barely influenced by anthropic aerosols. Its importance lies in the fact that the aerosol load
63 in the atmosphere above Reunion Island is under the influence of many different sources of emission and
64 dynamical processes responsible for short and long-range air-mass transports (Baray et al., 2013) such as biomass
65 burning (BB) plumes (Edwards et al., 2006; Khaykin et al., 2020), which are emitted seasonally in the SH.
66 Moreover, it is not rare for volcanic aerosols to be detected in the stratosphere above Maïdo observatory. In fact,
67 several volcanoes are located at the same latitude (Hunga-Tonga), or in the same Hemisphere (Calbuco) as Reunion
68 Island (Bègue et al., 2017; Khaykin et al., 2017; Tidiga et al., 2022; Baron et al., 2023; Sicard et al., 2023). The
69 high altitude of this facility is also of great importance as it is located above the boundary layer during the night,
70 allowing the observation of the free troposphere in a quasi-pristine environment.

71 Since its creation in 2012, the Maïdo facility has been equipped with four research lidar (light detection and
72 ranging) instruments emitting electromagnetic radiations at different wavelengths. Three of them have been
73 providing high resolution time series of aerosol extinction and backscatter vertical profiles in the UV (355 nm)
74 and visible (532 nm) domains. As of today, these measurements have only been used occasionally for case studies
75 (Bègue et al., 2017; Khaykin et al., 2017; Tidiga et al., 2022; Baron et al., 2023; Sicard et al., 2023). Full
76 exploitation of these timeseries will enable to provide timeseries of aerosol extinction and backscatter profiles over
77 Reunion Island. This can only be achieved after homogenizing the processing method for the three instruments.

78 This works provides a summary of the specifications of the systems and a full description of the preprocessing
79 and processing methods used to produce different levels of the datasets for the three Maïdo lidars.

80 **2. Instrumental description**

81 **Table 1** is a summary of the characteristics of the three Maïdo lidars used to retrieve aerosol optical properties. A
82 full description of each system is available in the following subsections.

83

a supprimé: scarcely

2

	Li1200		LiO3S	LiO3T		
References	(Dionisi et al., 2015; Vérèmes et al., 2019)		(Portafaix et al., 2015)	(Duflot et al., 2017)		
Time-series	In 2013-2017 2017-ongoing		2013-current	In 2013-2017 2017-ongoing		
Laser	2 × Quanta-Ray Nd: YAG pro-290		1 × Quanta-Ray Nd: YAG Lab-150	1 × Quanta-Ray Nd: YAG Pro-290		
Emitted wavelength (nm)	355		355	532		1064
Frequency (Hz)	30		30	30		
Energy (mJ/pulse)	375		150	250		
Reception channels (nm)	Elastic 355M, 355H Raman 387	Elastic 355VL, 355L Raman 387L	Elastic 355H, 355M Raman 387M	Elastic 532//, 532⊥	Elastic 532H, 1064 Raman 607	
Telescope diameter (mm)	1 × 1200	+ 1 × 200	4 × 500	1 × 200	+ 1 × 500	
Full overlap (km)	~ 15	~ 15	~ 4-5	~ 4-5	~ 4-5	
Detectors	Hamamatsu Photomultiplier tube (PMT)		Hamamatsu PMT	Hamamatsu PMT		Photodiode (1064nm)
Detector mode	Photocounting		Photocounting Analog (355M)	Photocounting Analog (532H, 1064)		
Filter bandwidth (nm)	1	1.3 (355VL) 1.3 (355L) 3 (387L)	1	1	0.7 (532H) 1.6 (607.7) *4 (1064)*	
Raw vertical resolution (m)	15		120 (2012 → 2017) 15 (2017 → current)	7.5		
Acquisition	Licel transient recorders					
Raw files integration time (minute)	1		3 (2012 → 2017) 1 (2017 → 2022)	2		
Reception channels (nm)	355H, 355M, 387	+ 355L, 355VL + 387VL	355H, 355M, 387	Elastic // 532 Elastic ⊥ 532	+ 532H	+ 607.7 *+ 1064*
Observation capabilities (Range, km)	15-45	3-25	10-45	4-25	10-45	4-15

Table 1: Systems technical features. The letters VL, L, M and H after the wavelength stand for Very Low, Low, Medium and High, respectively. Only aerosol channels are listed here.

2.1.   Lidar 1200 (Li1200)

The Li1200 is a Rayleigh Raman lidar able to measure vertical profiles of temperature between 30 and 100 km asl and water vapor ratio from the ground up to 18 km (Vérèmes et al., 2019). Vertical profiles of aerosol light extinction and backscattering can also be retrieved from the raw signals, as this instrument provides Rayleigh-Mie scattering at 355 nm and Raman N_2 scattering at 387 nm. This instrument has been operating at the Maïdo facility since 2012 and produces data since 2013.

(i)   Actual configuration

The emission consists in two Nd: YAG lasers Pro-290, Quanta-Ray Pro Series, from Spectra-Physics, emitting electromagnetic pulses at 1064 nm and 30 Hz (https://www.laserlabsource.com/files/pdfs/solidstatelasersource_com/product-305/Nd_Yag_Laser_Nanosecond_Laser_1064nm_1250mJ_Spectra_Physics-1462086952.pdf). The final

109 wavelength emitted is 355 nm, which corresponds to the third harmonic of the initial wavelength. Each pulse
110 delivers 375 mJ in 9 ns. The optical design of this lidar is represented in **Figure 1**. The two laser beams are
111 recombined through a polarizer cube, then sent to the telescope through a series of mirrors. It should be noted that
112 the lasers and the telescope are not in the same room, hence the use of many mirrors. BE1 and BE2 lenses form
113 an afocal of magnification 1.25, reducing the divergence of the beams and mixing the phases. The goal is to reduce
114 the hot spots, especially on the very fragile optic BE3. Last, the laser beam is channeled through the center of the
115 main telescope and magnified by a factor of 10 thanks to the afocal system BE3 and BE4. The emission and main
116 reception are therefore static coaxial, reducing the parallax effect and the minimum overlap altitude.

117 **The reception** is made of two telescopes. The main telescope consists in a primary mirror of 1200 mm diameter
118 (M1200), which gave its name to this instrument. A secondary mirror HM sends the beam to the detection system.
119 The L1 lens allows the beam to converge faster, which explains the 3.6 m value of the focal length. GS1 is a glass
120 plate that sends about 8 % of the beam on the 355 nm Very Low (355VL channel) detector. As this detector is
121 located before the FD2 diaphragm, its field of view is the same as the one of the telescope, and it receives signal
122 in the very near-range. A density (ND) was placed in front of this detector to avoid saturation. FD2 is a diaphragm,
123 located at the focal plane of the telescope. Its aperture improves the geometrical factor of the telescope for the
124 detectors following it. DM1 is a dichroic filter that reflects 355nm and allows 387nm and 407nm to pass through.
125 GS2 is a glass plate that sends about 8% of the beam on the 355 nm Medium (355M) channel and 92% of the beam
126 on the 355nm Hight (355H) channel. DM3 is a dichroic filter which selects the 387 nm for the Raman N2 channel.
127 As of 2017, a second telescope, with a 200 mm M200 primary mirror and a focal length of 1 m, sends the signal
128 to a second detection box, using an optical fiber. This detection box filters the Rayleigh and Raman signals and
129 channels them respectively to the 355L and 387L detectors.

130 All the **detectors** are photomultiplier tubes (PMT) from Hamamatsu, reconditioned by the Licel company
131 (https://www.hamamatsu.com/content/dam/hamamatsu-
132 photonics/sites/documents/99_SALES_LIBRARY/etd/PMT_TPMZ0002E.pdf). The 355H, 355M, and 355L
133 detectors are electronically shuttered to prevent saturation. The **acquisition** cards also come from Licel and operate
134 in photocounting mode. There are no analog channels. Raw files follow a 1-minute integration.

135 **To summarize**, 355M and 355H channels exist since 2013, but their acquisition starts at 15 and 25 km,
136 respectively, to avoid saturation. Hence, the 355VL and 355L channels were added in 2017 to cover the first
137 altitude ranges below 15 km. The minimum height for 355L electronic shuttering is 450 m asl.

138 *(ii) Previous modifications*

139 The detection unit was modified in 2017. Before that, the detection unit containing the 355L and 387VL
140 detectors did not exist. The M1200 mirror separation unit was modified. First, the part containing the FD1 to L3
141 optics, as well as the 355VL detector, did not exist. And there was an optic between IF2 and DM2 that would send
142 the visible signal to another detection unit. Indeed, originally, this lidar was supposed to operate at two emission
143 wavelengths, 355 and 532nm. However, during installation, due to mechanical and optical problems, only the 355
144 nm channel was retained (Dionisi et al., 2015).

Lasers :
λ = 355 nm
f = 30 Hz
E (1 laser) = 375 mJ/pulse
Θ = 0,5 mrad

Beam propagation :
C1 : Polarizing cube beamsplitter
M1, ..., M8 : Rmax 355 nm

Beam expander X1,25 :
BE1 : Lens (f = -200mm)
BE2 : Lens (f = 250mm)

Beam expander X12 :
BE3 : Convex mirror (f = 75mm)
BE4 : Parabolic mirror (f = 900mm)

Telescopes :
M1200 : Primary mirror (Ø=1,2m, f = 3,6m)
HM : Hexagonal mirror
M200 : Primary mirror (Ø=0,2m, f = 1,06 m)
OF : Optical fiber (Ø = 1,5 mm)

T200 wavelength separation unit :
L8 : Lens (f = 50mm)
DM4 : Longpass filter 376nm (FF376-Di01)
IF4 : Bandpass filter 355-1,3nm (FF01 356/30-25)
IF5 : Bandpass filter 386,7-3,0nm
L9, L10 : Lenses (f = 30mm)

Photomultipliers tubes :
355L : R9880-113G (BKA0493)
387L : R9880-113 (BKA0481)

T1200 wavelength separation unit :
L1 : Barlow Lens (f = -100mm)
GS1, GS2 : Glass slides 94/6
FD1 : Field Iris Diaphragm Ø = 5 mm
L2, L4 : Lenses (f = 200mm)
ND : Neutral density filter
IF1 : Bandpass filter 355-1,3nm (LL01-355-25)
L3, L7 : Lenses (f = 30mm)
L5, L6 : Lenses (f = 100mm)
FD2 : Field Iris Diaphragm Ø = 2 mm
DM1 : High-pass filter 360nm (360AELP)
IF2 : Bandpass filters 354,7-1,0nm
DM2 : High-pass filter 370nm (370AELP)
DM3 : High-pass filter 402nm(402-502-ULTRA)
IF3 : Bandpass filter 386,7-1,0nm

Photomultipliers tubes :
355VL : R7400P-03 (HC2228)
355M : R7400P-03G (HB9398)
355H : R7400P-03G (HB9577)
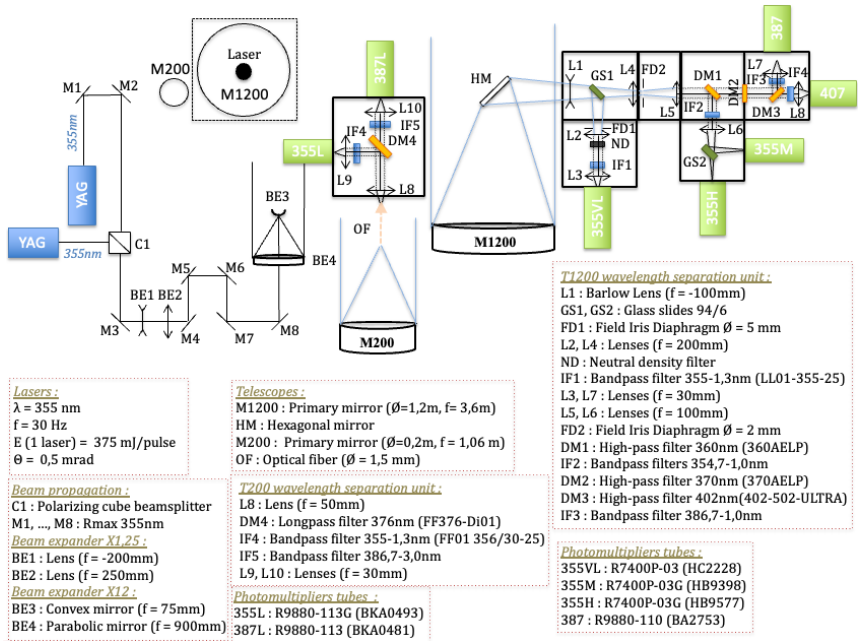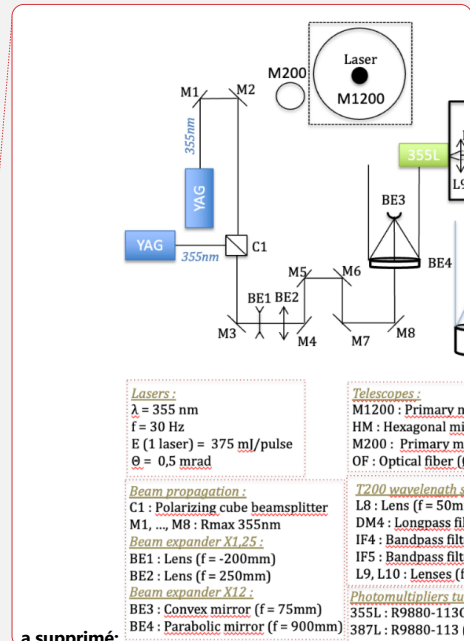387 : R9880-110 (BA2753)

Figure 1 : Li1200 optical scheme

2.2. Stratospheric Ozone Lidar (LiO3S)

The Stratospheric Ozone Lidar (LiO3S) works with the DIfferential Absorption Lidar (DIAL) technique and provides vertical profiles of ozone (O_3) concentration in the stratosphere, between the tropopause and about 45 km (Godin-Beekmann et al., 2003; Portafaix et al., 2003). To this end, two different wavelengths are emitted: a 308 nm signal strongly absorbed by ozone molecules and a 355 nm signal weakly absorbed by ozone molecules. Vertical profiles of aerosol light extinction and backscattering can be retrieved from the elastic scattering at 355 nm and Raman N_2 scattering at 387 nm. From 2000 to 2012, the LiO3S was located at the Moufia University campsite in Saint-Denis and provided ozone vertical profiles. It was moved to the Maïdo facility in 2012 and has been measuring from this location since 2013.

(i)   Actual configuration

The emission set-up consists in two different lasers. An excimer laser IPEX-840, PulseMaster PM-800 Series excimer laser with XeCl gas from LightMachinery (https://lightmachinery.com/lasers/excimer-lasers/ipex-800/), emits electromagnetic pulses at 308 nm with a frequency of 40 Hz and pulse energy of 220 mJ. A Nd: YAG laser Lab-150, Quanta-Ray Lab Series from Spectra-Physics emits electromagnetic pulse at a 1064 nm with a frequency of 30 Hz (https://www.laserlabsource.com/files/pdfs/solidstatelasersource_com/product-305/Nd_Yag_Laser_Nanosecond_Laser_1064nm_1250mJ_Spectra_Physics-1462086952.pdf). The final wavelength emitted by the Nd: YAG laser is 355 nm, corresponding to the third harmonic of the emitted wavelength. The pulse energy at this wavelength is 130 mJ. The laser beam diameter is about 10 mm, and its divergence is 0.5 mrad. The optical design of this lidar is represented in **Figure 2**. Again, the emission and reception

174 of this lidar are located in different rooms, explaining the use of many mirrors. The expander consists in three
175 lenses, BE1, BE2 and BE3, magnifying the signal by a factor 10. The final beam has a 100 mm diameter.

176 **The reception** is made of four 500 mm diameter telescopes. The primary mirrors are M1, M2, M3 and M4.
177 The signal is emitted at the center of these telescopes, and the distance between the emission and the center of each
178 telescope is 600 mm. At the receiving end, the signal is a focused from each telescope to a corresponding optical
179 fiber, which are positioned in line before entering the detection box. In this box, a diffraction grating separates the
180 different wavelengths. Internal mirrors allow the beam to be reflected in the detectors. Finally, a glass plate
181 discriminates the high and low energy channels at 355 nm.

182 All the **detectors** are photomultiplier tubes (PMT) from Hamamatsu, reconditioned by the Licel company
183 (https://www.hamamatsu.com/content/dam/hamamatsu-
184 photonics/sites/documents/99_SALES_LIBRARY/etd/PMT_TPMZ0002E.pdf), and the signal **acquisition** cards
185 are from Licel. The 355 nm detectors are electronically shuttered to avoid saturation. The acquisition is in
186 photocounting mode only for the high energy channels, and in photocounting and analog mode for the low energy
187 channels. Raw files follow a 1minute integration.

188 *(ii)   Previous modifications*

189 Before 2017, the electronic obturation concerned only 355H and 308H channels, and a mechanical chopper
190 shuttered 355M, 308M and Raman channels at the entrance of the detection box. In 2017, this chopper
191 malfunctioned and was replaced by electronic obturation for the 355M and 308M channel. Raman channels were
192 not shuttered anymore. The initial integration time was 3 minutes and was reduced to 2 and then 1 minute. During
193 this period, the vertical resolution was modified from 120 m to 15 m.
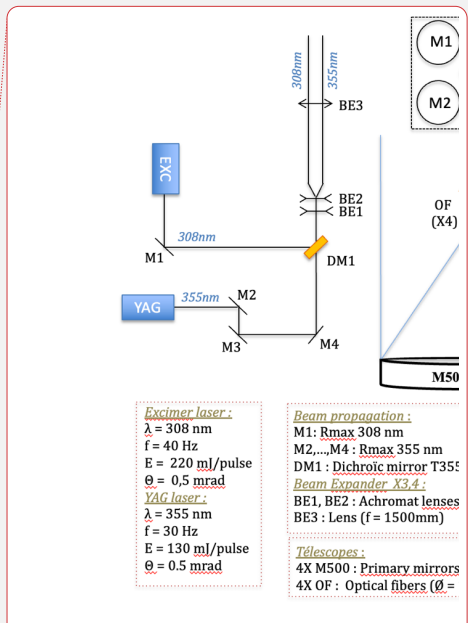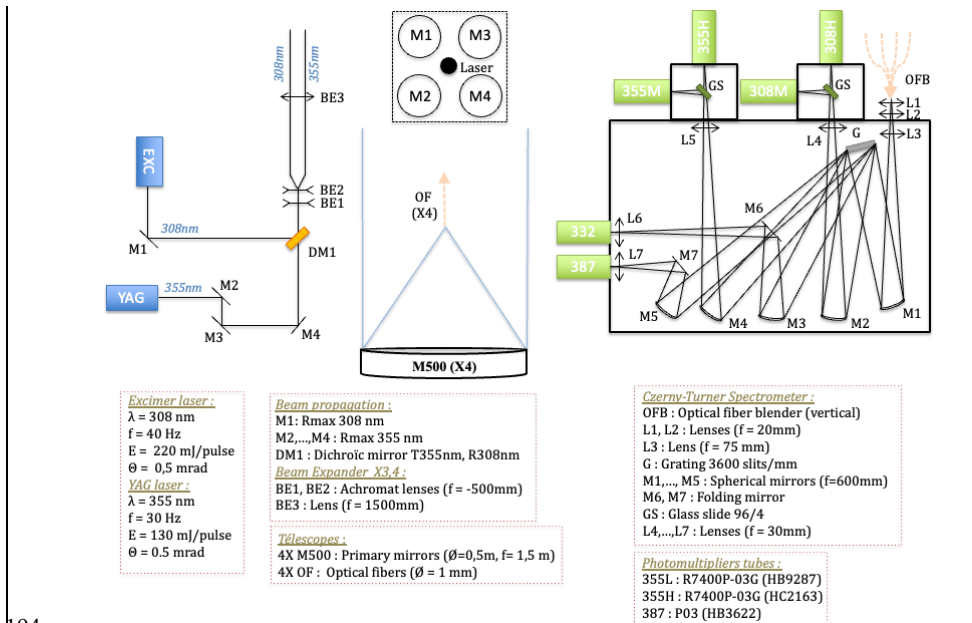
Figure 2 : LiO3S optical scheme

194

a supprimé: All the **detectors** are PMT from Hamamatsu and

a supprimé:

6

2.3.   Tropospheric Ozone Lidar (LiO3T)

The Tropospheric Ozone Lidar (LiO3T) also works with the DIAL technique and provides vertical profiles of ozone (O_3) concentration in the troposphere, between 6 and 25 km (Duflot et al., 2017). To this end, two different wavelengths are emitted using stimulated Raman scattering: a 289 nm signal strongly absorbed by ozone molecules and a 316 nm signal weakly absorbed by ozone molecules. Vertical profiles of aerosol light extinction and backscattering can be retrieved from the residual emission of the laser in terms of elastic scattering at 532 nm and 1064 nm, and Raman N_2 scattering at 607 nm. From 1993 to 2012, the LiO3T was located at the Moufia University campsite in Saint-Denis and provided ozone vertical profiles. It was moved to the Maïdo facility in 2012 and has been measuring from this location since 2013. The first aerosol dedicated polarized channels were installed in 2014.

(i)   Actual configuration

The emission consists in a Nd: YAG lasers Pro-290, Quanta-Ray Pro Series, from Spectra-Physics, emitting initially at 1064 nm at 30 Hz (https://www.laserlabsource.com/files/pdfs/solidstatelasersource_com/product-305/Nd_Yag_Laser_Nanosecond_Laser_1064nm_1250mJ_Spectra_Physics-1462086952.pdf). While the fourth harmonic (266 nm) is used to retrieve tropospheric ozone profiles (through its passage in a Raman cell generating 289 and 316 nm pulses), we use the second harmonic (532 nm) to retrieve aerosol light extinction and backscattering. Each pulse at 532 nm provides an energy of 250 mJ. The laser beam diameter is of about 10 mm, and its divergence is about 0.5 mrad. The optical design of this lidar for aerosol measurements is represented in **Figure 3**. Again, the emission and reception of this lidar are located in different rooms, explaining the use of many mirrors. The lenses, BE1, BE2 and BE3, magnify the signal by a 15 factor. The final emitted beam diameter is 100 mm.

The reception is made of two telescopes: one for the Rayleigh and Raman channels (532, 607 and 1064 nm, respectively), and the other for the polarized channels at 532 nm. The first telescope (M500) consists in a 500 mm diameter primary mirror. An optical fiber located at its focal point, conducts the signal to the detection box. Dichroic filters separate the 532, 607 and 1064 nm wavelengths. The second telescope consists in a 200 mm diameter primary mirror immediately followed by a polarizing cube. An optical fiber leads the polarized and cross-polarized beams to interference filters and to the detectors.

All the **detectors** are photomultiplier tubes (PMT) from Hamamatsu, reconditioned by the Licel company (https://www.hamamatsu.com/content/dam/hamamatsu-photonics/sites/documents/99_SALES_LIBRARY/etd/PMT_TPMZ0002E.pdf), except for the 1064 nm detector, which is an avalanche diode with a 3 mm diameter sensor (https://www.hamamatsu.com/content/dam/hamamatsu-photonics/sites/documents/99_SALES_LIBRARY/ssd/si_apd_kapd0001e.pdf). The 532 high energy channel (532H) detector is the only one electronically shuttered. All the **acquisition** cards are from Licel. The acquisition of the 532 nm polarized channel as well as the 607 nm channel are in photocounting mode. The acquisition of the 532H channel is in photocounting and analog modes, and the acquisition of the 1064nm channel is only in analog mode. Raw files follow a 2-minute integration.

(ii)   Previous modifications

**a supprimé:** Quanta Ray Pro 290 laser from Spectra-Physics …

a supprimé: .

a supprimé: All the **detectors** are PMT from Hamamatsu,

In 2014, the 200 mm telescope (M200) and the T200 wavelength separation unit were installed, allowing for the first aerosol measurements with polarized channels. In 2017, one of the four 500 mm telescopes initially dedicated to ozone measurements was used for aerosol measurements. A second detection box was added, enabling the 607 nm and 1064 nm channels acquisition.
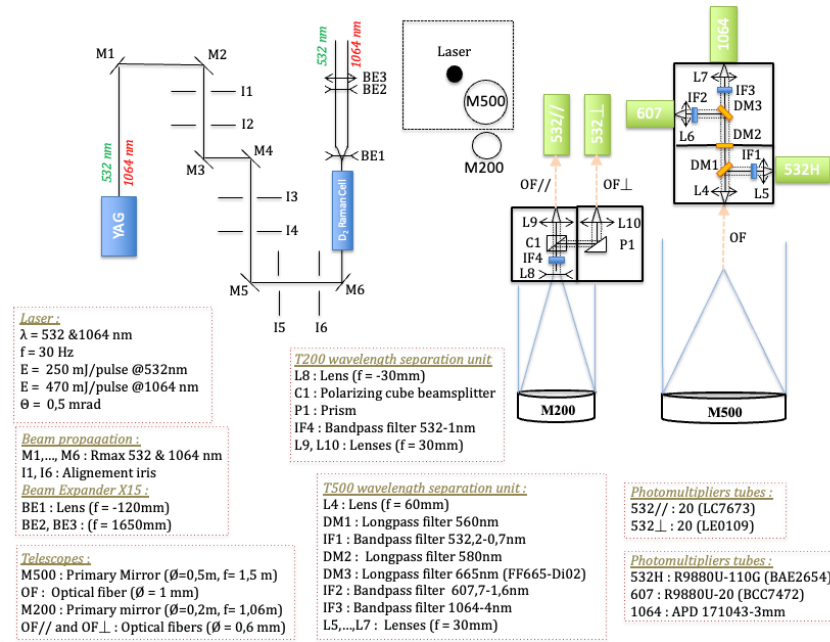
Figure 3 : LiO3T optical scheme
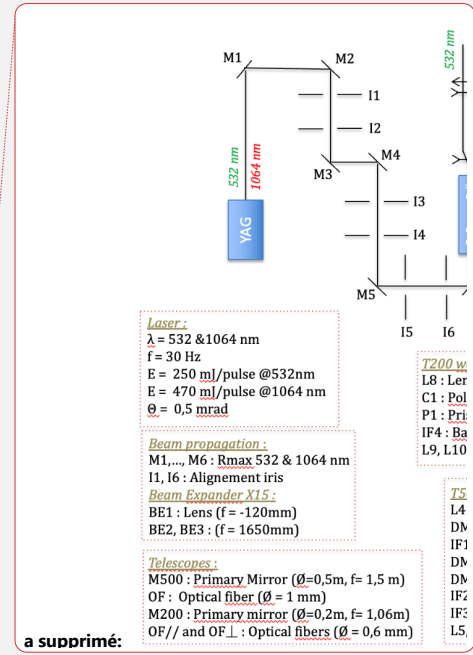
3. Routine measurements

The Maïdo lidars are research instruments that require manual handling and a constant human presence while operating. Maïdo observatory is a high-altitude facility (2160 m asl) and is located above the boundary layer in the free troposphere during the night. Acquisitions are only made during the night to increase the SNR. These instruments were originally intended to observe data in the stratosphere and the upper troposphere, so they are optimized to work at night, to improve the SNR up to very high in the atmosphere. That is why acquisitions are only made during the night. Measurements also require the absence of low-clouds or rain. The position of the Maïdo observatory on the west side of Reunion Island often protects the site from the clouds brought by trade winds. Notably, a ceilometer was installed at the Maïdo facility in 2019 and continuous observations revealed an average cloud frequency of respectively 20% and 40% during winter and summer nights (not shown).

Routinely, Maïdo lidars are operated two nights per week and measurements last from 7pm to 1am (local time, i.e. from 15 to 21 UTC). Specific campaigns (once or twice a year) can occasionally require to significantly increase the number of measurements. Operating these instruments implies to follow a strict, well-prepared protocol including basic check-ups and laser power control. A metadata file is routinely fed with technical specifics

for each night of observation and after any instrumental modification. Automatization is currently in progress and could increase the frequency of routine measurements.

Maïdo lidars are large and cannot be moved to make horizontal measurements: the beams of the different lidars are always vertical. To avoid any problems with flying objects, a no-fly zone around the Observatory is requested before each lidar measurement and during operating hours (exclusively nighttime). The research building hosting these instruments has a restricted access. It is located far from any residential areas. The instruments themselves can only be accessed by trained authorized personnel equipped with personal protective equipment (including eye protection glasses for the laser wavelengths) and Optical Enclosures.

4. Data processing chain

4.1. Data processing levels

Our datasets follow a classification detailed in the following description. Data processing levels range from Level 0 to Level 2.

 (i) Level 0 products (L_0) are uncorrected and uncalibrated raw data files in Licel format at full resolution produced by the instrument.

 (ii) Level 1 products (L_1) provide cloud-free data cleaned from any instrumental artifact (electronic parasites, synchronization problems, power disrupt, etc.). The cloud mask is currently manual. These corrections are essential for any user to be able to apply their own specific aerosol preprocessing without errors linked to the instrument itself or the weather.

 (iii) Level 2 products (L_2) provide processed lidar data including: saturation correction, background-sky correction, geometrical form factor correction and gluing between high and low-energy channels. These products also provide the aerosol optical properties and their corresponding uncertainties.

4.2. L_0 to L_1 processing chain

Each instrument is equipped with an acquisition system provided by the Licel firm. The description of the acquisition program producing output files in Licel format can be downloaded at *http://licel.com/raw_data_format.html*. This process concerns three main sources of interferences: **(i)** Detection-related interferences, **(ii)** Acquisition problems and **(iii)** Interferences linked to the lidar environment.

Any significative step of this process is tagged in the L1a output files to identify the corrections applied.

4.2.1. Detection interferences

Detection-related interferences can generally be linked to electromagnetic disturbances, which can occur in three different ways.

(i) An increased background signal concerning variable altitude ranges can impact the complete profile as shown in **Figure 4a**. This disturbance affects one or several channels across a significant altitude range, making the data acquisition unusable and requiring its withdrawal. The strong disturbance in the signal made it easy to fully automatize their detection. Notably, obturated detectors are more sensitive to these disruptions. Experience proved that they are directly related to the use of cell phones and Talky-Walkies. These instruments have been

303 banned from the instrumental rooms during the measurements, significantly decreasing the frequency of these
304 cases.

305 **(ii)** A second electronic problem often encountered comes from electronic gating. In fact, if a high and low-
306 energy channel coexist, a peak can be observed on the low-energy channel raw signal, at the gated altitude of the
307 high-energy channel (**Figure 4b**). This parasite peak usually appears on 2 consecutive range bins. This type of
308 problem occurs when the detectors are obturated and can have a significant impact on the measurement. It is
309 therefore necessary to remove the corresponding values and replace them by an averaged value between the
310 previous and following range bins.

311 **(iii)** The third detection disturbance corresponds to a sudden peak of the signal on a single randomly located
312 range bin. They only concern LiO3S and LiO3T. The consequence on the nighttime averaged profile is shown on
313 **Figure 4c**. Generally, the intensity of these spurious peaks is consistent and significantly higher than the
314 atmospheric background noise. They are easily identified when the intensity of the received signal is much lower
315 and become negligible with a stronger signal. However, there is an intermediate zone where the intensity of the
316 received signal is close to the intensity of these peaks, making their detection more challenging. They are replaced
317 by an averaged value.

318
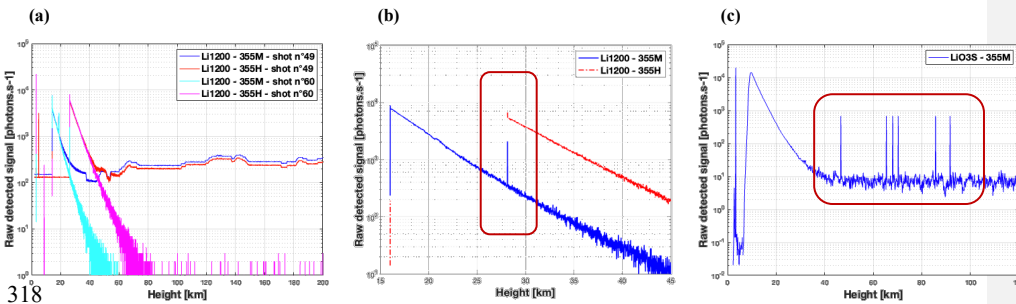
319 **Figure 4: (a) Raw Li1200 signal: background signal anomaly, (b) Raw Li1200 signal: peak from electronic gating, (c) Raw LiO3S nighttime averaged signal: random peaks in the far-range.**

4.2.2. Acquisition problems

321 The acquisition program computes 1- or 2-minute integrated profiles, depending on the instrument. However,
322 with this acquisition program, the measurement cannot be stopped at the end of the current cycle. As a result, the
323 last file is generally shorter than the others and must be removed to guarantee consistent measurements.

324 Another issue was a time desynchronization of several minutes between the computer acquisition clocks in
325 2021, revealing a configuration default in the corresponding Network Time Protocol time servers. Time differences
326 could increase up to 15 minutes between the different computers. This default has been fixed and a time-correction
327 is applied for signals between 2012 and 2021.

328 Last, interaction between the different lidars working at the same time and emitting the same wavelength can
329 also lead to interferences and disturbances on sensitive channels. To avoid this issue, the lasers are synchronized
330 out of phase. However, errors with this offset can lead to files with a higher sky background than others. These
331 files are removed.

4.2.3. Disturbance from clouds.

10

333   The SNR is most sensitive to the presence of low-altitude clouds. These clouds strongly absorb the emitted
334   photons and lead to high extinction levels and weak SNRs. They must be removed. High-altitude cirrus clouds can
335   also be removed if stratospheric aerosols are studied. Cloud-detection can be both automatic and/or manual. An
336   automatic detection of low clouds under 5 km height has been developed and can be used from 2019 up to now
337   using data from a Campbell CS135 ceilometer set up at the Maïdo facility in 2019. A manual cloud screening is
338   done for any remaining cirrus or low clouds. Automatization is in progress for this time-consuming work.

339   ### 4.3.   L₁ to L₂ processing chain

340   The goal of this second processing chain is to retrieve vertical profiles of aerosol optical products. It involves
341   several key steps.

342   #### 4.3.1.   Saturation correction

343   Saturation affects photomultiplier tube detectors with an acquisition card in photocounting mode. It concerns
344   the lower layers of the atmosphere and appears when the number of backscattered photons overcomes the capacity
345   of the acquisition card to discriminate them individually. Therefore, the backscattered signal is attenuated in the
346   corresponding layers. On the contrary, acquisition in analog mode is not affected by saturation, but has a weaker
347   SNR.

348   One solution is to combine (namely glue) analog and photocounting channels if both are available, which is
349   not always the case for our instruments.

350   The second option is to compare high and low-energy channels (or analog and photocounting channels if
351   available) in the lower layers and apply a dead-time correction to the photocounting channel using the Müller
352   equation. This is the solution we adopted for Maïdo lidars concerning aerosol, which is similar to what is done
353   for ozone and temperature processings (Leblanc et al., 2016a; Leblanc et al., 2016b). The dead-time parameter
354   (τ_d) corresponds to the minimum time for discriminating two consecutive photons. Our photocounting modes are
355   non-extensive, which means that the dead-time value is independent from the number of backscattered photons.
356   We then apply the Müller equation (Müller, 1973):

357
$$S_{desat} = \frac{S_{sat}}{1 - \tau_d \cdot \frac{c}{2.\,\delta_z.\,L} \cdot S_{sat}} \quad (1)$$

358
359   With S_{sat} (resp. S_{desat}) corresponding to the saturated (resp. desaturated) detected signal in number of photons
360   per second, δ_z the vertical resolution in meters, c the light celerity in meters per second, and L the number of shots.

361   A value of $\tau_d = 3.7 ns$ is chosen. This value is the one recommended by Licel manufacturers and was confirmed
362   after several experimental tests which are available in a summary document.

363   #### 4.3.2.   Background correction

364   The background sky signal (S_{BC}), is one of the main sources of noise affecting the SNR. It corresponds to: **(i)**
365   the detector noise, and **(ii)** the natural light emitted by the atmosphere and can be affected by the presence of the
366   moon during the night. The value of this signal is supposed to be constant with the altitude but in practice it
367   sometimes follows a linear variation due to the effect of the signal induced noise on the detector. Our instruments
368   are not equipped with any pre-trigger. Our method to calculate the (S_{BC}) value consists in performing a linear

369 regression or an averaging of the desaturated signal in an altitude range high enough to neglect the impact of the
370 backscattered signal compared to the (S_{BC}), typically between 80km and 120km.

4.3.3. Geometrical form factor correction

372 The overlap function $F_{(z)}$ or crossover function is one of the major sources of uncertainties for ground-based
373 lidar measurements. It describes the fraction of the laser beam cross section contained by the telescope field of
374 view as a function of range. Its values vary between 0 (blind zone, no overlap) and 1 (full overlap). Originally,
375 Maïdo lidars were designed to study the high troposphere and the stratosphere and at these altitudes, the full overlap
376 is obtained, which is why there has not yet been a more specific study on these instruments.

377 Should this parameter not be corrected, the received lidar signal would be attenuated between the blind zone
378 and the full overlap, leading to incorrect optical values. Two approaches can be followed to determine this
379 parameter. **(i)** A theoretical calculation using equations found in Measures (1984) can be performed. However, it
380 implies the knowledge of several optical parameters which can vary over the timeseries, and different equations
381 must be used for coaxial and biaxial systems. **(ii)** The second and most common approach is experimental and
382 implies the use of horizontal measurements (Chazette et al., 2017). In fact, considering a constant and homogenous
383 atmosphere along the line of sight, a linear regression can be performed in an altitude range high enough to be far
384 from the full overlap. The difference between the logarithm of the signal and this linear regression gives an accurate
385 estimation of $F_{(z)}$.

$$F_{(z)} = \exp\left(\ln\left(S_2(z)\right) - y(z)\right) \quad (2)$$

387 With S_2 the desaturated, background corrected, and range corrected lidar signal, $y(z)$ the linear regression and
388 z the altitude range.

389 It is physically impossible for these research instruments to measure horizontally. Therefore, the experimental
390 approach using vertical measurements (instead of horizontal) in aerosol-free conditions was performed to correct
391 overlap for the very low and low channels of the lidar 1200. As of today, no overlap correction was needed for the
392 LiO3S (full overlap under 10km) and LiO3T (full overlap between 3 and 4km).

393 **Figures 5a and 6a** reveal the variability of the overlap function over the time-series for both Li1200 VL and
394 L channels. This variability can be explained by slight misalignments of the lidar. Indeed, given the important
395 number of optical elements between the laser and the emission point, the risk of misalignment, even minor, is
396 significant. **Figures 5b and 6b** show the mean and standard deviation (std) of the overlap function from an
397 exponential regression. The small values of std are an indicator of a low-varying function, a result that allows to
398 use a unique overlap function rather than different functions for different periods. The estimated altitude of full
399 overlap was 10 km for the Very Low channel and 15k m for the Low channel.

(a)   (b)
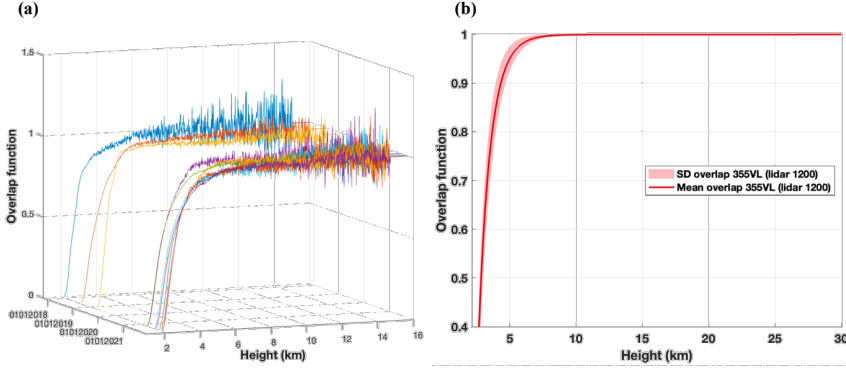
Figure 5: Li1200 VL channel. (a) Time series of overlap functions, (b) Mean and standard deviation of the overlap function.

(a)   (b)
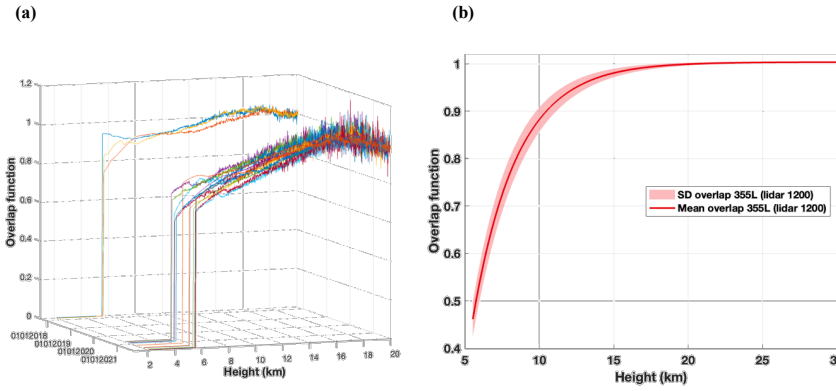
Figure 6: Li1200 L channel. (a) Time series of measured overlap functions, (b) Mean and standard deviation of the exponential regression of the overlap function.

4.3.4. Smoothing

Smoothing is applied on the lidar signal to increase the accuracy of the retrieved aerosol profiles. For the three time-series, smoothing was achieved using a low-pass filter with a Blackman window (Blackman and Tukey, 1958). The number of points for the filter was altitude-dependent and channel-dependent.

$$S_{filt}(z) = S_2(z)/F(z) * \frac{coef}{\sum coef} \quad (3)$$

$$coef(n) = 0.42 - 0.5 * cos\left(\frac{2\pi n}{W-1}\right) + 0.08 * cos\left(\frac{4\pi n}{W-1}\right), 0 \leq n \leq M-1 \quad (4)$$

With S_{filt} the smoothed signal, S_2 the desaturated, background corrected, and range corrected lidar signal, M half the length of the window and W the weight of the filter.

Figures 7a-c represent the new vertical resolution for each channel of each instrument. Two methods can be used to estimate vertical resolution after smoothing: **(i)** Impulse response method and **(ii)** Digital Filter. The latter was chosen for these time-series. It involves the mathematical calculation of the filter transfer function, using a cut-off frequency at -3dB (NDACC_resolDF, (Leblanc et al., 2016)).
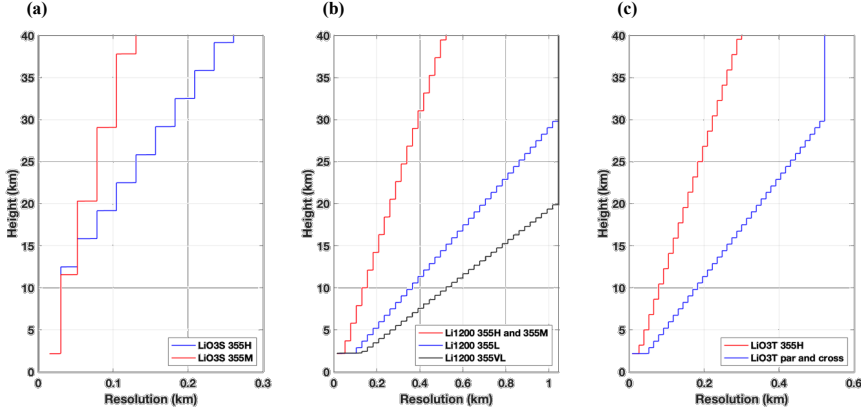
13

418

419

420 **Figure 7: NDACC vertical resolution of (a) LiO3S, (b) Li1200, and (c) LiO3T.**

421 ### 4.3.5. Gluing near and far-range channels

422 High and low energy channels were combined for the LiO3S and the Li1200 using the gluing method of the
423 square sinus and cosinus functions. The altitude range chosen for the gluing corresponded to a region where the
424 high energy channel was not affected by electronic distortions and the low energy channel was not affected by too
425 much noise.

$$
426 \quad \begin{cases} v1_{(z)} = 0, & z < altmin \\ v1_{(z)} = \sin^2\left(\frac{0 \xrightarrow{n} 1}{n} * \frac{\pi}{2}\right), & altmin \leq z \leq altmax \end{cases} \quad (5)
$$

$$
427 \quad \begin{cases} v2_{(z)} = 1, & z < altmin \\ v2_{(z)} = \cos^2\left(\frac{0 \xrightarrow{n} 1}{n} * \frac{\pi}{2}\right), & altmin \leq z \leq altmax \end{cases} \quad (6)
$$

428 With n the number of range bins between $altmin$ and $altmax$, $v1$ the vector to apply to the high energy channel
429 and $v2$ the vector to apply to the low energy channel.

430 The channels glued and used for inversion were: **(i)** 355VL + 355L + 355M + 355H and 355L + 355M + 355H
431 and 355M + 355H for the Li1200, and **(ii)** 355H + 355M for the LiO3S. Each of these glued channels is available
432 in the L_{1b} files. Inversion was applied for each glued channels and corresponding optical products can be found in
433 the L_2 files.

434 ### 4.3.6. Calibration depolarization value for the LiO3T

435 Polarization channels enable to detect changes in the backscattered polarization state produced by the
436 atmospheric particles. The laser provides quasi pure linear polarization. A polarizing cube beam splitter transmits
437 the received linear polarized light and reflects the received cross polarized light. It is necessary to determine the
438 polarization calibration factor before combining the two signals (Biele et al., 2000).

439 Three methods can be used: **(i)** Rayleigh calibration method (Behrendt and Nakamura, 2002), **(ii)** $\pm45°$ or $\Delta90°$
440 calibration methods (Freudenthaler, 2016), and **(iii)** 3 signals (total, cross and parallel) method (Reichardt et al.,

14

441 2003). While methods 2 and 3 provide the smallest uncertainties, method 1 can be used retrospectively if no total
442 channel existed. The apparent Volume Linear Depolarization Ratio (VLDR*) can then be calculated following:

$$VLDR^* = \frac{K}{\eta^*} * \frac{S_r}{S_t} \quad (7)$$

446 With t and r the respective transmitted and reflected parts of the signal S, η^* the apparent calibration factor and K
447 the calibration factor correction parameter.

448 The VLDR can then be computed using the polarization crosstalk parameters for the transmitted and reflected
449 signals ($G_{t,r}$ and $H_{t,r}$):

$$VLDR = \frac{VLDR^*(G_t + H_t) - (G_r + H_r)}{(G_r - H_r) - VLDR^*(G_t - H_t)} \quad (8)$$

453 The total signal will also be reconstructed following:

$$S_{total} = \frac{\frac{\eta^*}{K}H_r S_t - H_t S_r}{H_r G_t - H_t G_r} \quad (9)$$

457 The aerosol backscatter β_a will then be deduced from the total signal S_{total} using Klett inversion. The backscatter
458 ratio R will be calculated following:

$$R = \frac{(\beta_a + \beta_{mol})}{\beta_{mol}} \quad (10)$$

462 Finally, the Particle Linear Depolarization Ratio ($PLDR$) can be computed following:

$$PLDR = \frac{(1 + LDR_{mol}) * VLDR * R - (1 + VLDR) * LDR_{mol}}{(1 + LDR_{mol}) * R - (1 + VLDR)} \quad (11)$$

466 In our case, we used the Rayleigh method before 2017 and the 3 signals method after 2017. We used a linear
467 molecular depolarization ratio (LDR_{mol}) of 0.00398 at 532nm (Behrendt and Nakamura, 2002) to estimate η^*, and
468 a K factor of 1 to estimate $VLDR^*$. Crosstalk parameter values were considered ideal: $G_t = 1$, $H_t = 1$, $G_r = 1$ and
469 $H_r = -1$.

4.3.7. Optical products: Klett inversion

471 This step is mandatory to retrieve aerosol optical properties from the detected lidar signals. However, it implies
472 to resolve an order 1 Bernoulli equation with several unknown parameters. Several methods exist such as: (i) One
473 or two-components Klett inversion (Klett, 1981, 1985), (ii) Raman inversion (Ansmann et al., 1990, 1992), and
474 (iii) a synergistic method using Klett inversion and sunphotometer measurements to evaluate the lidar ratio (Raut
475 and Chazette, 2007).

15

476 Because Raman channels have currently a very low SNR, they are not included in this work and the two-
477 component Klett inversion method was chosen for the three systems. It implies to determine an *a priori* constant
478 value of Lidar Ratio (LR) and a clean, aerosol-free zone in the atmosphere (Rayleigh zone). Details about the
479 elastic two-component algorithm from Klett are available in **Appendix A**.

480 The solution proposed in Appendix A is:

481

482
$$\beta(\lambda, z) = \beta_a(\lambda, z) + \beta_m(\lambda, z) = \frac{S_2(\lambda, z) \cdot \exp\{2 \cdot \int_{z'=z}^{z_{ref}} \left(\frac{LR_a(\lambda, z')}{LR_m(\lambda, z')} - 1\right) \cdot \alpha_m(\lambda, z') dz'\}}{\frac{S_2(\lambda, z_{ref})}{\beta(\lambda, z_{ref})} + 2 \cdot \int_{z'=z}^{z_{ref}} LR_a(\lambda, z') \cdot S_2(\lambda, z') \cdot \exp\{2 \cdot \int_{x'=z}^{z_{ref}} \left(\frac{LR_a(\lambda, x')}{LR_m(\lambda, x')} - 1\right) \cdot \alpha_m(\lambda, x') dx'\} \cdot dz'} \quad (12)$$

483

484 With a (resp. m) the particular (resp. molecular) contribution, $\alpha(\lambda, z)$ (resp. $\beta(\lambda, z)$) the summed molecular and
485 particular extinction (resp. backscatter), and **LR** the Lidar Ratio. S_2 corresponds to the range-corrected, sky
486 background corrected and desaturated signal. However, the signal used in this study for the inversion algorithm is
487 smoothed as explained in paragraph 4.3.4. and could be glued (Li1200, LiO3S) or recombined (LiO3T).

488 Several unknown parameters must be determined:

489 (i)   To retrieve the **LR$_a$**, we chose a constant LR value of 50 sr for the three instruments to be consistent
490   between the time-series and to target the most frequent aerosol types. Moreover it enables easier
491   comparisons with satellite data such as CALIOP products (Cattrall et al., 2005).

492 (ii)   The equation used to retrieve the molecular extinction was (Bates, 1984):

493
$$\alpha_m(\lambda, z) = \frac{P}{k * T} * \frac{4.02.10^{-28}}{\lambda^{4+(0.389\lambda + 0.09426\lambda^{-1} - 0.3228)}} \quad (13)$$

494   With k corresponding to the Boltzmann constant. Atmospheric pressure P and temperature T were
495   retrieved from the Arletty AERIS product *(https://www.aeris-data.fr/)*, relying on data from the
496   European weather forecast model ECMWF (European Centre for Medium-Range Weather Forecasts),
497   and producing interpolated data every 6h around Maïdo observatory (Hauchecorne, n.d.).

498

499   The molecular backscatter was then computed following:

500

501
$$\beta_m(\lambda, z) = \alpha_m(\lambda, z) * \frac{3 * K_f}{8\pi} \quad (14)$$

502   The King factor's value (K_f) is considered equal to 1 (King, 1923), and $\frac{3}{8\pi}$ corresponds to the **LR$_m$**.

503 (iii) The last step was to determine for each daily measurement and each channel a reference 'Rayleigh'
504   zone z_{ref} supposed free of any aerosols.

505

4.3.8.   Raman and 1064 nm channel issues

507 Klett inversion brings the problem of considering a lidar ratio constant with height. In fact, a single aerosol
508 plume is often made of several layers of particles with heterogenous backscattered lidar signals. Raman inversion
509 is one solution to deduce a vertical profile of lidar ratio from elastic and Raman channels. However, our Raman
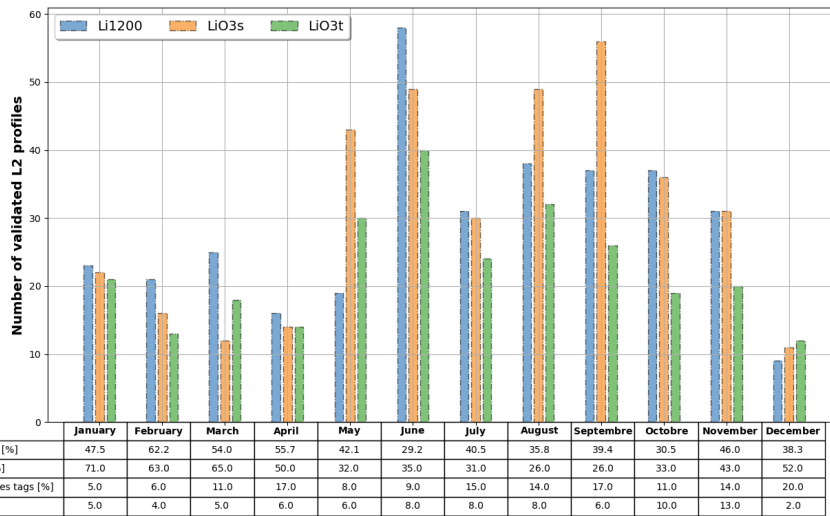
channels have a poor SNR and are not usable for stratospheric or high tropospheric aerosols. The retrieval of aerosol optical products using Raman inversion for low-energy channels (low and middle troposphere) is still ongoing. There is also a misalignment issue for the 1064-nm channel leading to a poor SNR. This channel is currently unexploitable.

5. Quality assessment

5.1. Database statistics

A total of 1737 nighttime measurements were preprocessed between 2013 and 2023: 710 files for Li1200, 534 files for LiO3S, and 493 files for LiO3T. Notably, the mean percentage of rejected files was higher for Li1200 (52.7%), than LiO3T (44.8%) and LiO3S (32.7%). **Figure 8** shows the cumulated monthly number of validated L_2 profiles for each instrument, the monthly mean number of rejected files and corresponding tags (cloud detection, technical issue, low SNR). It should be noted that most observations were made during the May to November period (austral winter, dry season) compared to the December to April period (austral summer, wet season), which is consistent with the higher cloud and rain occurrence during the wet season. The mean percentage of validated L_1 files was 62.4% during the dry season and 48.5% during the wet season. The lower frequency of measurements in January, July, August, and December also concurs with two important holiday periods. The frequency of technical issues and lower SNR is statistically higher during the months with a greater number of measurements.

	January	February	March	April	May	June	July	August	Septembre	Octobre	November	December
Rejected files [%]	47.5	62.2	54.0	55.7	42.1	29.2	40.5	35.8	39.4	30.5	46.0	38.3
Cloud tags [%]	71.0	63.0	65.0	50.0	32.0	35.0	31.0	26.0	26.0	33.0	43.0	52.0
Technical issues tags [%]	5.0	6.0	11.0	17.0	8.0	9.0	15.0	14.0	17.0	11.0	14.0	20.0
SNR tags [%]	5.0	4.0	5.0	6.0	6.0	8.0	8.0	8.0	6.0	10.0	13.0	2.0

Figure 8: Number of validated files for the three instruments in the period 2013-2023. In the table below, mean percentage of rejected files and tagged files for each month.

5.2. Instrumental capabilities

The gluing technique allowed to determine different altitude ranges for each lidar depending on the channels available. **Table 1** provides a summary of the theoretical instrumental performances in terms of altitude ranges. Apart from the number of glued channels, other parameters can influence the maximum altitude (SNR) or the minimum altitude (Overlap, SNR) of the validated L_2 vertical profile. The LiO3T at 532 nm is ideal to investigate

17

534 the low and mid troposphere. The high troposphere and stratosphere can be studied at 355 nm (Li1200 and LiO3S)
535 or 532 nm (LiO3T – from 2017 until now).

5.3. Instrumental intercomparison

537 In this study, we performed a comparison between the three instruments to detect any major discrepancies
538 using the Stratospheric Aerosol Optical Depth (sAOD) between 17 and 30 km. **Figure 9** displays the time-series
539 of sAOD at 355 nm (Li1200 and Li03S) for concomitant measurements and corresponding uncertainties. There is
540 a good overall consistency between the two instruments. The differences between the two time-series could be the
541 consequence of technical modifications (channel addition, optimization, misalignments). Three peaks periods of
542 high sAOD values can be identified: the emission of volcanic aerosols in the stratosphere during the Hunga-Tonga
543 eruption in 2022 (Kloss et al., 2022; Baron et al., 2023; Sicard et al., 2023), the Calbuco volcanic eruption in 2015
544 (Bègue et al., 2017) and the Australian bushfires in 2020 (Khaykin et al., 2020). Higher differences in 2021 could
545 be the consequence of repeated misalignments for the Li1200.
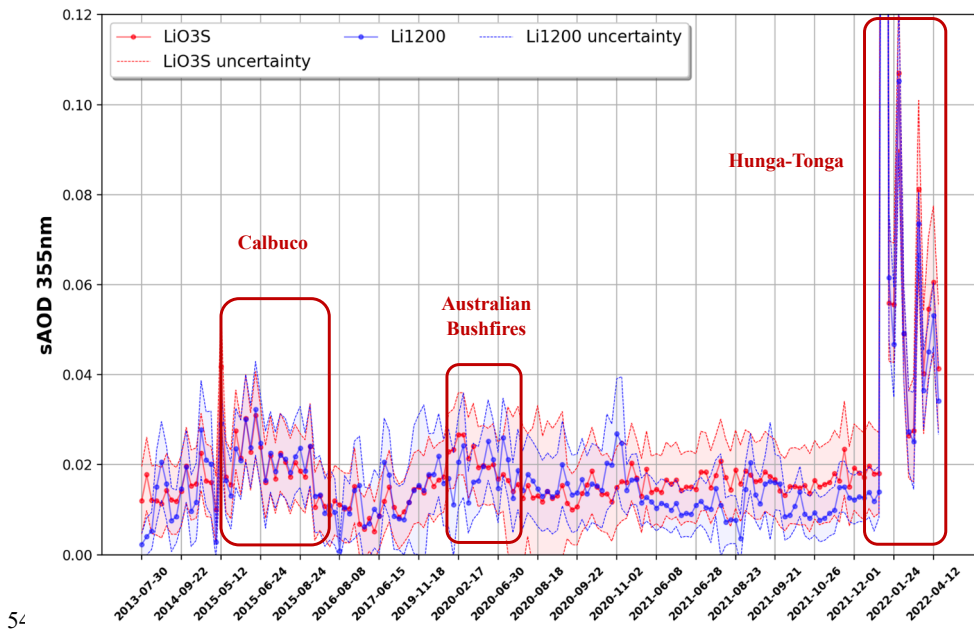
Figure 9: Nighttime AOD (17 to 30 km layer) at 355 nm, from the Li1200 (red) and LiO3S (blue) (concurrent measurements) with corresponding uncertainties (dashed colored lines). Exceptional events circled in red. The horizontal timeline is not linear: one date out of eight is represented for visual purposes.

548 The dispersion of sAOD values is represented in **Figure 10**. The sAOD at 355 nm varies between 0.001 and
549 0.107 for LiO3S and Li1200, with a mean of 0.019 ± 0.012 and 0.017 ± 0.012 , respectively. A good correlation
550 is found between the two lidars (correlation R = 0.924 ± 0.005).
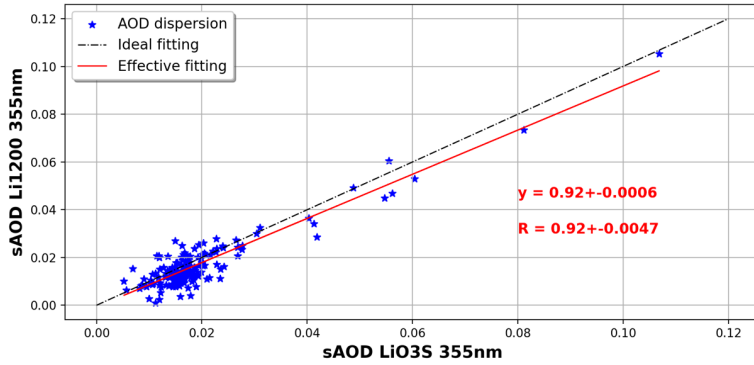
Figure 10: Dispersion of the AOD (17 to 30 km layer) at 355 nm, between the Li1200 and LiO3S. The red line represents the theoretical linear regression.

The correlation between the two instruments at 355 nm in terms of extinction values is higher above 17 km but lower from 10 to 17 km (**Appendix D**, **Figure D1**). In fact, for the Li1200: **(i)** low energy channels were added in 2017, **(ii)** there were changes in the minimal altitude of detection for the 355M channel, and **(iii)** this instrument had many misalignments and underwent several optical upgrades, leading to modifications of the overlap function.

For further retrospective trend studies, it is important to note that the LiO3S has been the most stable instrument throughout the time-series and is considered the reference instrument at 355 nm. However, data from the Li1200 can be used to fill the gaps of the LiO3S database depending on the altitude range targeted, but also for specific case studies with the need to retrieve optical products for the middle and low troposphere.

The same analysis was performed for the LiO3T. To compare the two wavelengths, Ångström exponents (AE) were computed between the LiO3T (532 nm) and alternatively the LiO3S (355 nm) and Li1200 (355 nm). **Figure 11** shows the dispersion of AE values. The order of magnitude of AE values varies between 0.0794 and 1.288 with a mean of 0.56 ± 0.29 and 0.54 ± 0.28, respectively. Again, a good correlation is found between both datasets ($R = 0.901 \pm 0.128$). These values also demonstrate the variability of stratospheric aerosol size distribution between 17 and 30 km (Gobbi et al., 2007; Burton et al., 2012).
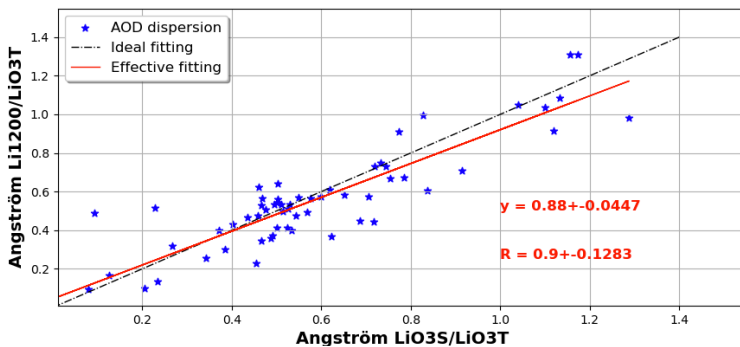
Figure 11: Dispersion of the AE (17 to 30 km layer) between 355 and 532 nm. The black line represents the theoretical linear regression and the red line the actual linear regression.

19

Table 2 summarizes the metrics used to intercompare the three instruments. The relative Mean Bias Error (MBE) was added the analysis. After identifying the LiO3S as the reference instrument at 355 nm, we found a negative MBE (- 6.55 %) concerning sAOD, meaning that the Li1200 tends to underestimate sAOD compared to LiO3S.

	Relative Mean Bias Error	Linear Regression Slope	Correlation coefficient
sAOD	- 7.59 %	0.92	0.92 ± 0.0047
Ångström exponent	- 6.55 %	0.88	0.90 ± 0.1283

Table 2: Intercomparison between the three instruments in terms of sAOD and Ångström exponent.

5.4.   Main sources of uncertainties

The total uncertainty budget of each lidar is described in **Appendix B**. Four sources of uncertainty were propagated in quadrature (Sicard et al., 2009; Rocadenbosch et al., 2010): **(i)** uncertainty due to the Rayleigh calibration value (u_{altref}), **(ii)** uncertainty due to the lidar ratio value (u_{LR}) with a distinction between *LR, top* and *LR, bottom* defining the respective upper and lower error bars, **(iii)** uncertainty due to the SNR vertical distribution (u_{SNR}), **(iv)** and uncertainty due to the SNR value at the calibration altitude ($u_{SNR,altref}$). **Figures 12a-12c** represent for three case reports the importance of each uncertainty relatively to the total backscatter in percentage, and **Figures 12d-12f** represent the corresponding propagated total backscatter uncertainty for the three instruments.

In **Figures 12a-12c,** the behavior of the uncertainties u_{altref} (blue curves) and $u_{SNR,altref}$ (green curves) is stable over the different altitude ranges. Notably, u_{altref} comes from the 5% uncertainty of the molecular backscatter, which determines the lower threshold for the total uncertainty. The u_{SNR} uncertainty (purple curves) is strongly influenced by the altitude, with minimal values at lower altitude ranges where the lidar signal is stronger, and values increasing with the altitude. In fact, lidar signals are filtered before inversion, making u_{SNR} the predominant error at higher altitude levels. Oppositely, the u_{LR} uncertainty (orange and yellow curves) is the lowest at the calibration altitude and increases in the lower levels, where it becomes predominant. The systematic uncertainty on the LR value was set to 30% for this study. Therefore, the total uncertainty is the lowest in mid-altitude ranges before increasing in lower and higher altitude levels. Sharp spikes in u_{LR} can be observed just below 20km for the LiO3S and Li1200, and below 8 km for the LiO3T. They are linked to the presence of aerosol plumes and emphasize the impact of aerosols on the uncertainty values in lower altitude levels.

For the LiO3S (H+M glued channel), the total relative uncertainty reaches 15% at 10 km, decreases down to 6% around 20 km, and increases up to 8% around 35 km. (**Figure 12a**). Without the aerosol layer, the minimum error would be reached around 15 km. For the Li1200 (H+M+L+VL glued channel), the total relative uncertainty reaches 20% at 7 km and decreases down to 5% from 20 km up. (**Figure 12b**). The uncertainty due to the SNR is very low compared to the LiO3S, as this instrument is designed to reach very high-altitude levels, and the signal used for inversion is made of four filtered signals with complementary vertical capacities. Without the aerosol layer, the minimum error would be reached around 17 km. For the LiO3T, the total relative reaches 10% at 4 km, decreases down to 6% around 8 km, and increases up to 20% around 25 km. (**Figure 12c**). The uncertainty due to the SNR is higher than the previous lidars because this instrument is designed for tropospheric measurements.
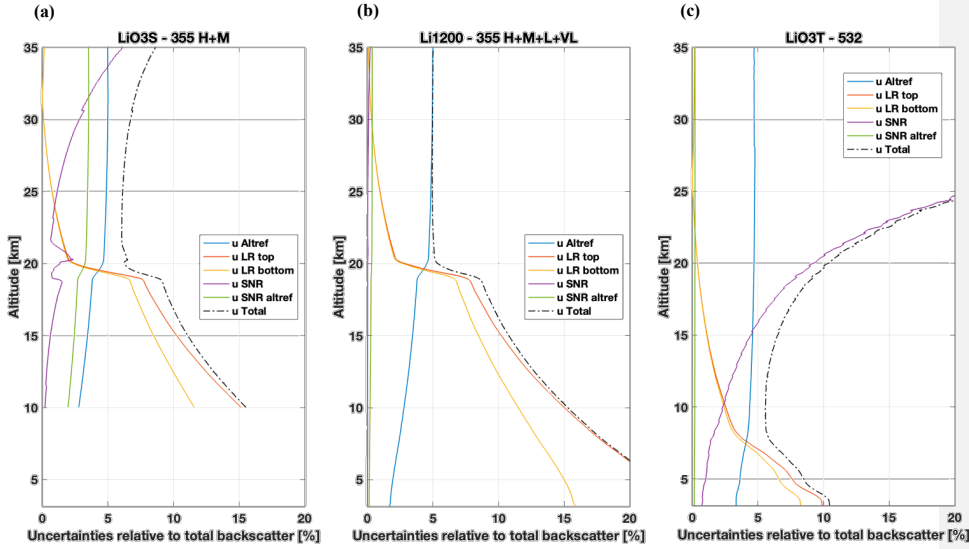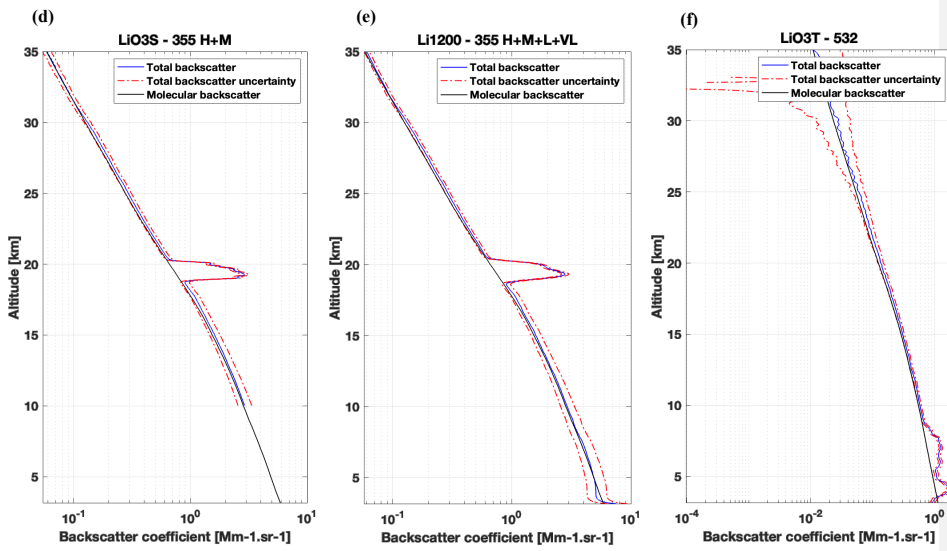
Figure 12: Upper row: random cases showing the molecular backscatter (black), the backscatter coefficient (blue) and its apparent uncertainty (red dotted line) for the (a) LiO3S (25/01/2022), (b) Li1200 (25/01/2022) and (c) LiO3T (25/09/2017). Lower row: corresponding relative uncertainties for the (d) LiO3S, (e) Li1200 and (f) LiO3T.

In **Figures 12d-12f**, the three instruments demonstrate their capacity to detect aerosol layers with relatively low error rates and a high resolution. **Figures 12d-12e** specifically show their ability to identify variations within the aerosol layer between 18 and 20 km. For the LiO3T (**Figures 12f**), the aerosol layer between 4 and 8 km is exceptionally well defined, with relatively low error values. Apart from these aerosol layers, the molecular backscatter (in black) tends to align closely with the uncertainty of the total backscatter (in red). In fact, background

aerosols are characterized by very low backscatter and extinction values, leading to the relatively high sAOD uncertainties observed in **Figure 9**: higher for background aerosols but lower for cases with a stronger aerosol load, such as from Australian fires or volcanic aerosols. Focusing on the uncertainty specific to aerosol backscatter (rather than the total) is essential to improve the uncertainty analysis, along with a statistical analysis of the dataset to minimize disruptions caused by transient aerosol events. Time-series of aerosol backscatter relative total uncertainties were computed for the three instruments and the corresponding mean and standard deviation are represented **Figures 13a-c**. Values are high and easily reach 100% for the three instruments because of the very low values of aerosol backscatter coefficients above Maïdo observatory. The mean uncertainty is the lowest for the LiO3S between 18 and 25 km (64.4± 31.6 %). It increases under 18 km and above 25 km with relative uncertainty values reaching more than 100% due to the very weak aerosol backscatter values at these altitude ranges. The mean uncertainty for the Li1200 is also the lowest between 18 and 25 km (50.3 ± 29.0 %). It increases under 18 km and above 25 km with relative uncertainty values relatively lower than the LiO3S due to a lower SNR, and the presence of low and very low channels detecting aerosol plumes at lower altitudes. The LiO3T exhibits a low relative uncertainty below 20 km, it varies around 69.1 ± 42.7 %. The strong increase above 20 km is essentially explained by the very low SNR for this instrument at these altitude ranges.
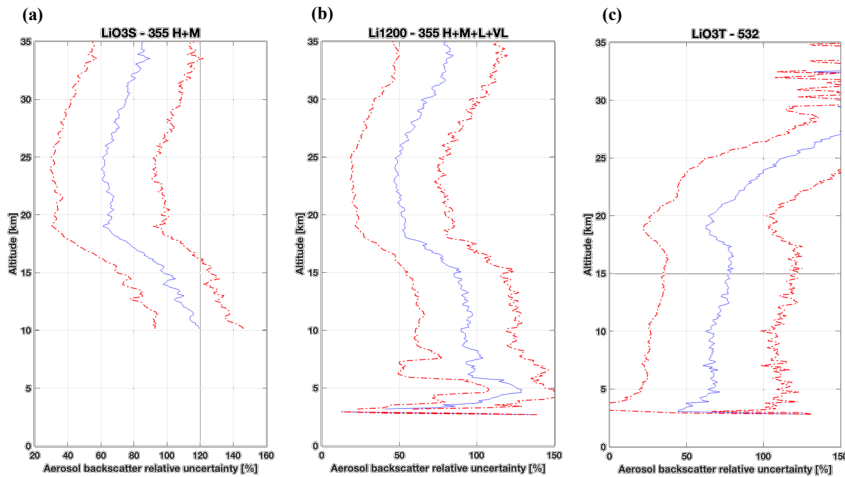
Figure 13: Mean (blue line) and standard deviation (dotted red line) of the time-series of relative uncertainty from the inversion technique for the (a) lidar O3S (H+M channel), (b) lidar 1200 (H+M+L+VL channel) and (c) lidar O3T (polarized channels).

Table 3 provides a summary of the processing method and the area of validity of the Level 2 products.

	Li1200		LiO3S	LiO3T	
Time-series	In 2013-2017	2017-ongoing	2013-current	In 2013-2017	2017-ongoing
Elastic reception channels (nm)	355H, 355M	+ 355L, 355VL	355H, 355M	Elastic // 532 Elastic ⊥ 532	+ 532H
Geometrical form factor correction method	-	From vertical measurements	-	-	-
Polarization calibration method	-		-	Rayleigh method	3 signals method
Inversion method	Klett				
Vertical resolution range (km)	0.030 – 0.522	0.015 – 0.522	0.030 – 0.261	0.052 – 0.522	
Detection lower bound (km)	10	3	10	3	10
Detection upper bound (km)	45	45	40	25	35
Uncertainty averaged lowest values (%)	50.3 ± 29.0		64.4± 31.6	69.1 ± 42.7	

Table 3: Summary of the processing method and area of validity for the Level 2 products.

6. Data availability

Raw L_0 files, cleaned L_1 files and processed L_2 files with optical products are generated locally. L_0 files are made of 1minute integrated raw files in licel format. L_1 products contain 1-minute integrated time-series and overnight averaged cleaned signals in mat file format and netcdf format. L_2 products in mat file format contain overnight averaged processed signals, as well as range-corrected signals for Raman channels. L_2 products are also computed in netcdf format following NDACC guidelines in anticipation for a future NDACC label request. **Table C1** in **Appendix C** summarizes the optical products and other variables available in these L_2 netcdf files.

Each of these files is available on request in our local datacenter by FTP (ftp://tramontane.univ-reunion.fr/). L_1 and L_2 files are currently available at https://doi.org/10.26171/rwcm-q370 (Gantois et al., 2024). Mat files and netcdf files with L_2 data will soon be available on AERIS database, but only L_2 netcdf files will be openly accessible.

7. Summary

This study supports the first ever long-term time-series of multiwavelength aerosol optical properties generated from three lidars operating at the Observatory of Atmospheric Physics of La Réunion (OPAR) since 2013. A full description of the technical specifications for the three instruments is provided, as well as details about the preprocessing and processing methods used to produce the different dataset levels. The three time-series consist in vertical profiles of aerosol elastic backscatter and extinction coefficients at 355 and 532 nm, and linear depolarization ratio at 532 nm above Maïdo observatory (2160 m asl, west side of Reunion Island, Southern Hemisphere) from 2013 until now.

The preprocessing step required manual cleaning of more than 1700 files, and the highest frequency of cloud occurrence resulted in a lower number of validated profiles during the wet season. Data processing methods and the Klett inversion technique chosen for this work are detailed and referenced. One issue concerns the random misalignments and technical modifications for the three instruments leading to highly variable parameters such as the geometrical form factor. As an alternative to the Klett method, the Raman inversion technique has been attempted but failed for stratospheric and high tropospheric levels due to a poor SNR.

23

667   Intercomparison between the three instruments show a good correlation in terms of sAOD values. The
668   uncertainty analyses reveal a strong influence of the LR value in the low-altitude ranges and a strong influence of
669   the SNR in the high-altitude ranges. Uncertainty values relative to the total backscatter coefficient are low for the
670   three instruments. Uncertainty values relative to the aerosol backscatter coefficient are high for the three
671   instruments because of the very low aerosol backscatter coefficient values generally observed above Maïdo
672   observatory. Among the three instruments, the LiO3S stands out as the most stable (less misalignments, less
673   technical modifications) and should be considered the reference instrument at 355 nm. However, data from the
674   Li1200 can be used to fill the gaps of the LiO3S database and for specific case studies.

675   **Appendices**

676   **Appendix A**

677   The equation describing the desaturated lidar signal can be written as:

678
$$S_{desat}(\lambda, z) = C(\lambda) \cdot \frac{F(z)}{(z - z_0)^2} \cdot \left\{ \sum_i \beta_i(\lambda, z) \right\} \cdot \left\{ exp\left[-\frac{2}{\cos(\theta)} \cdot \sum_i \tau_i(\lambda, z_0, z) \right] \right\} + S_{bck}(\lambda) \quad (A1)$$

679   With C the instrumental constant, F the overlap function, β_i the backscatter coefficient of the component i, τ_i the
680   integrated extinction coefficient of the component i between altitude z_0 and z, and S_{bck} the background signal.

681   The range-corrected, sky background corrected and desaturated signal can then be considered:

682

683
$$S_2(\lambda, z) = [S_{desat}(\lambda, z) - S_{bck}(\lambda, z)] \cdot (z - z_0)^2 \quad (A2)$$

684

685   Derivation of the logarithm of S_2 leads to:

686

687
$$\frac{\delta[ln(S_2)]}{\delta z} = \frac{1}{\beta(\lambda, z)} \cdot \frac{\delta[\beta(\lambda, z)]}{\delta z} - 2 \cdot LR_a(\lambda, z) \cdot \beta(\lambda, z) - 2 \cdot \alpha_m(\lambda, z) \cdot \left(1 - \frac{LR_a(\lambda, z)}{LR_m} \right) \quad (A3)$$

688

689   With a (resp. m) the particular (resp. molecular) contribution, $\alpha(\lambda, z)$ (resp. $\beta(\lambda, z)$) the summed molecular and
690   particular extinction (resp. backscatter), and LR the Lidar Ratio:

691
$$LR_a(\lambda, z) = \frac{\alpha_a(\lambda, z)}{\beta_a(\lambda, z)} \quad (A4)$$

692
$$LR_m(\lambda, z) = \frac{\alpha_m(\lambda, z)}{\beta_m(\lambda, z)} = \frac{8\pi}{3} * K_f \quad (A5)$$

693   With K_f corresponding to the King factor's value.

694   The two-component solution of this Bernoulli equation is:

695

24

696 $\beta(\lambda, z) = \beta_a(\lambda, z) + \beta_m(\lambda, z)$

697 $$= \frac{S_2(\lambda, z) \cdot \exp\{2 \cdot \int_{z'=z}^{z_{ref}} \left(\frac{LR_a(\lambda, z')}{LR_m(\lambda, z')} - 1\right) \cdot \alpha_m(\lambda, z')dz'\}}{\frac{S_2(\lambda, z_{ref})}{\beta(\lambda, z_{ref})} + 2 \cdot \int_{z'=z}^{z_{ref}} LR_a(\lambda, z') \cdot S_2(\lambda, z') \cdot \exp\{2 \cdot \int_{x'=z}^{z_{ref}} \left(\frac{LR_a(\lambda, x')}{LR_m(\lambda, x')} - 1\right) \cdot \alpha_m(\lambda, x')dx'\} \cdot dz'} \quad (A6)$$

698

699 **Appendix B**

700 The uncertainty budget was determined from the Klett elastic one components inversion technique. Mathematical

701 details can be found in (Rocadenbosch et al., 2010) for the total backscatter inversion uncertainty budget and

702 (Sicard et al., 2009) for the two components inversion uncertainty budget.

703 The Klett inversion was applied to the filtered signal following (see section 4.3.4.):

704 $$S_{filt}(z) = \frac{S_2(z)}{F(z)} * \frac{coef}{\sum coef} \quad (3)$$

705 Considering $C = \frac{coef}{\sum coef}$ and $S_{geo}(z) = \frac{S_2(z)}{F(z)}$, the uncertainty of the filtered signal followed the equation:

706 $$u_{filt}(z) = \sqrt{\left[\frac{\partial S_{filt}(z)}{\partial S_{geo}(z)} \cdot u_{S_{geo}}(z)\right]^2 + \left[\frac{\partial S_{filt}(z)}{\partial C} \cdot u_C(z)\right]^2} = \sqrt{\left[C(z) \cdot u_{S_{geo}}(z)\right]^2 + \left[S_{geo}(z) \cdot u_C(z)\right]^2} \quad (B1)$$

707

708 **Table B1** is a summary of the Total-Backscatter analytical error bars to compute in Klett's backward inversion

709 method.

Uncertainty source	Equation
Uncertainty due to the Rayleigh calibration value (u_{altref})	$u_{altref} = \left\|\left(\frac{\beta_j}{\beta_N}\right)^2 \frac{U_N}{U_j}\right\| \sigma_{\beta_N}$
Uncertainty due to the lidar ratio value (u_{LR})	$u_{LR} = \left\|\pm p \frac{2\beta_j^2}{U_j} G_j + p^2 \frac{4\beta_j^3}{U_j^2} G_j^2\right\|$ Where: $G_j = \sum_{i=j}^N w_i S_i U_i$
Uncertainty due to the SNR vertical distribution (u_{SNR}).	$u_{SNR} = \sqrt{\left(\frac{\beta_j}{U_j}\right)^2 \sigma_{U_j}^2 + \left(\frac{2\beta_j}{U_j}\right)^2 \sigma_{GU_j}^2}$ Where: $\sigma_{GU_j}^2 = \sum_{k=j}^N (w_k S_k)^2 \sigma_{U_k}^2$
Uncertainty due to the SNR value at the calibration altitude ($u_{SNR,altref}$).	$u_{SNR,altref} \approx \left\|\frac{\beta_j^2}{\beta_N U_j}\right\| \sigma_{U_N}$

710
711 **Table B1: Total-Backscatter analytical error bars from Klett's backward inversion method (from Rocadenbosch et al., 2010)**

712

713 With β_j the total backscatter at the altitude cell j, U_j the range-corrected signal at the altitude cell j, N the calibration

714 altitude cell, σ_{U_j} the uncertainty if the range-corrected signal U, σ_{β_j} the uncertainty of the total backscatter, S_j the

715 total lidar ratio.

716 The uncertainty of the total backscatter error bars $u_{\beta T}$ can then be written as:

25

717

$$u_{\beta T} = \sqrt{u_{altref}^2 + u_{LR}^2 + u_{SNR}^2 + u_{SNR,altref}^2} \quad (B2)$$

718

26

Variable	Dimension	Unit
CHANNELS_ID	channel	-
LATITUDE_INSTRUMENT	time	deg
LONGITUDE_INSTRUMENT	time	deg
STATION_HEIGHT	time	m_asl
DATETIME	time	MJD2K
DATETIME_START	time	MJD2K
DATETIME_STOP	time	MJD2K
INTEGRATION_TIME	time	h
WAVELENGTH_EMISSION	channel	nm
WAVELENGTH_DETECTION	channel	nm
ANGLE_VIEW_ZENITH	time, channel	deg
ACCUMULATED_LASER_SHOTS	time, channel	1
ALTITUDE	points	m_asl
AEROSOL_RETRIEVAL_METHOD	time	-
AEROSOL_BACKSCATTER_RATIO_BACKSCATTER	time, channel, points	1
AEROSOL_BACKSCATTER_RATIO_BACKSCATTER_UNCERTAINTY_COMBINED_STANDARD	time, channel, points	1
AEROSOL_BACKSCATTER_RATIO_BACKSCATTER_RESOLUTION_ALTITUDE_IMPULSE_RESPONSE_FWHM	time, channel, points	m
RANGE_INDEPENDENT_NORMALIZATION	time	m_asl
RANGE-CORRECTED_SIGNAL	time, channel, points	Photons.s-1
AEROSOL_BACKSCATTER_COEFFICIENT_DERIVED	time, channel, points	m-1.sr-1
AEROSOL_BACKSCATTER_COEFFICIENT_DERIVED_UNCERTAINTY_COMBINED_STANDARD	time, channel, points	m-1.sr-1
AEROSOL_BACKSCATTER_COEFFICIENT_DERIVED_RESOLUTION_ALTITUDE_IMPULSE_RESPONSE_FWHM	time, channel, points	m
PRESSURE_INDEPENDENT	points	hPa
TEMPERATURE_INDEPENDENT	points	K
AEROSOL_EXTINCTION_COEFFICIENT_DERIVED	time, channel, points	m-1
AEROSOL_ EXTINCTION _COEFFICIENT_DERIVED_UNCERTAINTY_COMBINED_STANDARD	time, channel, points	m-1
AEROSOL_ EXTINCTION _COEFFICIENT_DERIVED_RESOLUTION_ALTITUDE_IMPULSE_RESPONSE_FWHM	time, channel, points	m
AEROSOL_LIDAR_RATIO_INDEPENDENT	time, channel, points	sr
VOLUME_LINEAR_DEPOLARIZATION_RATIO	time, channel, points	1
VOLUME_LINEAR_DEPOLARIZATION_RATIO _UNCERTAINTY_COMBINED_STANDARD	time, channel, points	1
VOLUME_LINEAR_DEPOLARIZATION_RATIO _RESOLUTION_ALTITUDE_IMPULSE_RESPONSE_FWHM	time, channel, points	m
AEROSOL_LINEAR_DEPOLARIZATION_RATIO_DERIVED	time, channel, points	1
AEROSOL_LINEAR_DEPOLARIZATION_RATIO_DERIVED _UNCERTAINTY_COMBINED_STANDARD	time, channel, points	1
AEROSOL_LINEAR_DEPOLARIZATION_RATIO_DERIVED _RESOLUTION_ALTITUDE_IMPULSE_RESPONSE_FWHM	time, channel, points	m

Table C1: Variables available in the L₂ netcdf files

27

Appendix D
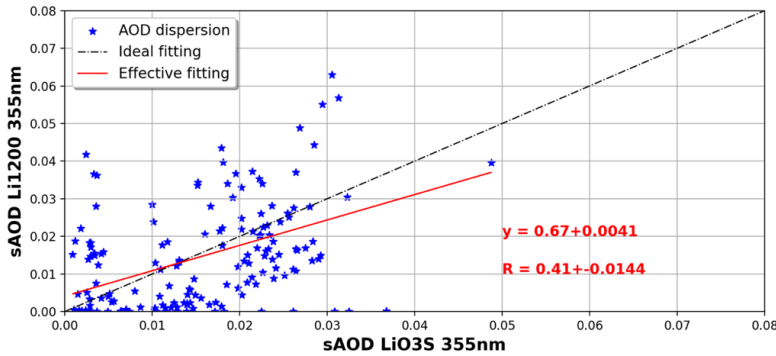
Figure D1: Dispersion of the AOD (10 to 17 km layer) at 355 nm, between the Li1200 and LiO3S. The black line represents the theoretical linear regression and the red line the actual linear regression.

Author contributions. DG conducted this study with the help of MS, GP, VD and NB. DG performed the processing of the lidar measurements, the uncertainty analysis, prepared the figures and the manuscript. GP and MS both contributed to the improvement of the text, figures, and uncertainty analysis of this manuscript. GP designed two original softwares used for data processing, which were improved by DG. NM designed the lidar optical schemes. TP and SGB were responsible for the LiO3S instrument and dataset, VD and NM were responsible for the LiO3T instrument and dataset, and VD and GP were responsible for the Li1200 instrument and dataset. PH and EG performed the lidar measurements and the instrumental maintenance and reviewed the technical aspects of this paper. All co-authors contributed to reviewing drafts of this manuscript.

Competing interests. The authors declare that they have no conflict of interest.

References

Alexander, L., Allen, S., Bindoff, N., Breon, F.-M., Church, J., Cubasch, U., Emori, S., Forster, P., Friedlingstein, P., Gillett, N., Gregory, J., Hartmann, D., Jansen, E., Kirtman, B., Knutti, R., Kanikicharla, K., Lemke, P., Marotzke, J., Masson-Delmotte, V., and Xie, S.-P.: Climate change 2013: The physical science basis, in: contribution of Working Group I (WGI) to the Fifth Assessment Report (AR5) of the Intergovernmental Panel on Climate Change (IPCC), in: Climate Change 2013: The physical science basis, 2013.

a supprimé:

Ansmann, A., Riebesell, M., and Weitkamp, C.: Measurement of atmospheric aerosol extinction profiles with a Raman lidar, Opt. Lett., 15, 746, https://doi.org/10.1364/OL.15.000746, 1990.

Ansmann, A., Wandinger, U., Riebesell, M., Weitkamp, C., and Michaelis, W.: Independent measurement of extinction and backscatter profiles in cirrus clouds by using a combined Raman elastic-backscatter lidar, Appl. Opt., 31, 7113, https://doi.org/10.1364/AO.31.007113, 1992.

Baray, J.-L., Courcoux, Y., Keckhut, P., Portafaix, T., Tulet, P., Cammas, J.-P., Hauchecorne, A., Godin-Beekmann, S., De Mazière, M., Hermans, C., Desmet, F., Sellegri, K., Colomb, A., Ramonet, M., Sciare, J., Vuillemin, C., Hoareau, C., Dionisi, D., Duflot, V., Vérèmes, H., Porteneuve, J., Gabarrot, F., Gaudo, T., Metzger, J.-M., Payen, G., Leclair De Bellevue, J., Barthe, C., Posny, F., Abchiche, A., Delmas, R., and Ricaud, P.: Maïdo observatory: a new high-altitude station facility at Reunion Island (21° S, 55° E) for long-term atmospheric remote sensing and in situ measurements, Atmospheric Meas. Tech., 6, 2865–2877, https://doi.org/10.5194/amt-6-2865-2013, 2013.

Baron, A., Chazette, P., Khaykin, S., Payen, G., Marquestaut, N., Bègue, N., and Duflot, V.: Early Evolution of the Stratospheric Aerosol Plume Following the 2022 Hunga Tonga-Hunga Ha'apai Eruption: Lidar Observations From Reunion (21°S, 55°E), Geophys. Res. Lett., 50, e2022GL101751, https://doi.org/10.1029/2022GL101751, 2023.

Bates, D. R.: Rayleigh scattering by air, Planet. Space Sci., 32, 785–790, https://doi.org/10.1016/0032-0633(84)90102-8, 1984.

Bègue, N., Vignelles, D., Berthet, G., Portafaix, T., Payen, G., Jégou, F., Benchérif, H., Jumelet, J., Vernier, J.-P., Lurton, T., Renard, J.-B., Clarisse, L., Duverger, V., Posny, F., Metzger, J.-M., and Godin-Beekmann, S.: Long-range transport of stratospheric aerosols in the Southern Hemisphere following the 2015 Calbuco eruption, Atmospheric Chem. Phys., 17, 15019–15036, https://doi.org/10.5194/acp-17-15019-2017, 2017.

Behrendt, A. and Nakamura, T.: Calculation of the calibration constant of polarization lidar and its dependency on atmospheric temperature, Opt. Express, 10, 805, https://doi.org/10.1364/OE.10.000805, 2002.

Biele, J., Beyerle, G., and Baumgarten, G.: Polarization Lidar: Correction of instrumental effects, Opt. Express, 7, 427, https://doi.org/10.1364/OE.7.000427, 2000.

Blackman, R. B. and Tukey, J. W.: BSTJ 37: 1. January 1958: The Measurement of Power Spectra from the Point of View of Communications Engineering - Part I. (Blackman, R.B.; Tukey, J.W.), 1958.

Burton, S. P., Ferrare, R. A., Hostetler, C. A., Hair, J. W., Rogers, R. R., Obland, M. D., Butler, C. F., Cook, A. L., Harper, D. B., and Froyd, K. D.: Aerosol classification using airborne High Spectral Resolution Lidar measurements – methodology and examples, Atmospheric Meas. Tech., 5, 73–98, https://doi.org/10.5194/amt-5-73-2012, 2012.

Cattrall, C., Reagan, J., Thome, K., and Dubovik, O.: Variability of aerosol and spectral lidar and backscatter and extinction ratios of key aerosol types derived from selected Aerosol Robotic Network locations, J. Geophys. Res. Atmospheres, 110, https://doi.org/10.1029/2004JD005124, 2005.

Chazette, P., Totems, J., Hespel, L., and Bailly, J.-S.: Principe et physique de la mesure lidar, vol. 1, ISTE, 209, 2017.

Dionisi, D., Keckhut, P., Courcoux, Y., Hauchecorne, A., Porteneuve, J., Baray, J. L., Leclair de Bellevue, J., Vérèmes, H., Gabarrot, F., Payen, G., Decoupes, R., and Cammas, J. P.: Water vapor observations up to the lower stratosphere through the Raman lidar during the Maïdo Lidar Calibration Campaign, Atmospheric Meas. Tech., 8, 1425–1445, https://doi.org/10.5194/amt-8-1425-2015, 2015.

Duflot, V., Baray, J., Payen, G., Marquestaut, N., Posny, F., Metzger, J.-M., Langerock, B., Vigouroux, C., Hadji-Lazaro, J., Portafaix, T., De Maziere, M., Coheur, P.-F., Clerbaux, C., and Cammas, J.-P.: Tropospheric ozone profiles by DIAL at Maïdo Observatory (Reunion Island): System description, instrumental performance and result comparison with ozone external data set, Atmospheric Meas. Tech., 10, 3359–3373, https://doi.org/10.5194/amt-10-3359-2017, 2017.

Edwards, D. P., Emmons, L. K., Gille, J. C., Chu, A., Attié, J.-L., Giglio, L., Wood, S. W., Haywood, J., Deeter, M. N., Massie, S. T., Ziskin, D. C., and Drummond, J. R.: Satellite-observed pollution from Southern Hemisphere

796   biomass burning, J. Geophys. Res., 111, D14312, https://doi.org/10.1029/2005JD006655, 2006.

797   Freudenthaler, V.: About the effects of polarising optics on lidar signals and the Δ90 calibration, Atmospheric
798   Meas. Tech., 9, 4181–4255, https://doi.org/10.5194/amt-9-4181-2016, 2016.

799   Gantois, D., Payen, G., Sicard, M., Duflot, V., Marquestaut, N., Portafaix, T., Godin Beekmann, S., Hernandez,
800   P., and Golubic, E.: Multiwavelength aerosol lidars at Maïdo Observatory, https://doi.org/10.26171/rwcm-q370,
801   2024.

802   Gobbi, G. P., Kaufman, Y. J., Koren, I., and Eck, T. F.: Classification of aerosol properties derived from
803   AERONET direct sun data, Atmospheric Chem. Phys., 7, 453–458, https://doi.org/10.5194/acp-7-453-2007, 2007.

804   Godin-Beekmann, S., Porteneuve, J., and Garnier, A.: Systematic DIAL lidar monitoring of the stratospheric ozone
805   vertical distribution at Observatoire de Haute-Provence (43.92°N, 5.71°E), J. Environ. Monit., 5, 57–67,
806   https://doi.org/10.1039/B205880D, 2003.

807   Hansen, J., Sato, M., and Ruedy, R.: Radiative forcing and climate response, J. Geophys. Res. Atmospheres, 102,
808   6831–6864, https://doi.org/10.1029/96JD03436, 1997.

809   Hauchecorne, A.: Ether, Service Arletty, Atmospheric Model Description, ETH-ACR-AR-DM-001, 22 pp., 1998.,
810   n.d.

811   Khaykin, S., Legras, B., Bucci, S., Sellitto, P., Isaksen, L., Tencé, F., Bekki, S., Bourassa, A., Rieger, L., Zawada,
812   D., Jumelet, J., and Godin-Beekmann, S.: The 2019/20 Australian wildfires generated a persistent smoke-charged
813   vortex rising up to 35 km altitude, Commun. Earth Environ., 1, 22, https://doi.org/10.1038/s43247-020-00022-5,
814   2020.

815   Khaykin, S. M., Godin-Beekmann, S., Keckhut, P., Hauchecorne, A., Jumelet, J., Vernier, J.-P., Bourassa, A.,
816   Degenstein, D. A., Rieger, L. A., Bingen, C., Vanhellemont, F., Robert, C., DeLand, M., and Bhartia, P. K.:
817   Variability and evolution of the midlatitude stratospheric aerosol budget from 22 years of ground-based lidar and
818   satellite observations, Atmospheric Chem. Phys., 17, 1829–1845, https://doi.org/10.5194/acp-17-1829-2017,
819   2017.

820   King, L. V.: The Complex Anisotropic Molecule in Relation to the Theory of Dispersion and Scattering of Light
821   in Gases and Liquids, Nature, 111, 667–667, https://doi.org/10.1038/111667a0, 1923.

822   Klett, J. D.: Stable analytical inversion solution for processing lidar returns, Appl. Opt., 20, 211,
823   https://doi.org/10.1364/AO.20.000211, 1981.

824   Klett, J. D.: Lidar inversion with variable backscatter/extinction ratios, Appl. Opt., 24, 1638,
825   https://doi.org/10.1364/AO.24.001638, 1985.

826   Kloss, C., Sellitto, P., Renard, J., Baron, A., Bègue, N., Legras, B., Berthet, G., Briaud, E., Carboni, E., Duchamp,
827   C., Duflot, V., Jacquet, P., Marquestaut, N., Metzger, J., Payen, G., Ranaivombola, M., Roberts, T., Siddans, R.,
828   and Jégou, F.: Aerosol Characterization of the Stratospheric Plume From the Volcanic Eruption at Hunga Tonga
829   15 January 2022, Geophys. Res. Lett., 49, https://doi.org/10.1029/2022GL099394, 2022.

830   Leblanc, T., Sica, R. J., van Gijsel, J. A. E., Godin-Beekmann, S., Haefele, A., Trickl, T., Payen, G., and Liberti,
831   G.: Proposed standardized definitions for vertical resolution and uncertainty in the NDACC lidar ozone and
832   temperature algorithms – Part 2: Ozone DIAL uncertainty budget, Atmospheric Meas. Tech., 9, 4051–4078,
833   https://doi.org/10.5194/amt-9-4051-2016, 2016a.

834   Leblanc, T., Sica, R. J., Van Gijsel, J. A. E., Haefele, A., Payen, G., and Liberti, G.: Proposed standardized
835   definitions for vertical resolution and uncertainty inthe NDACC lidar ozone and temperature algorithms – Part 3:
836   Temperatureuncertainty budget, Atmospheric Meas. Tech., 9, 4079–4101, https://doi.org/10.5194/amt-9-4079-
837   2016, 2016b.

838   Müller, J. W.: Dead-time problems, Nucl. Instrum. Methods, 112, 47–57, https://doi.org/10.1016/0029-
839   554X(73)90773-8, 1973.

840   Portafaix, T., Morel, B., Bencherif, H., Baldy, S., Godin-Beekmann, S., and Hauchecorne, A.: Fine-scale study of
841   a thick stratospheric ozone lamina at the edge of the southern subtropical barrier, J. Geophys. Res. Atmospheres,

30

842   108, 2002JD002741, https://doi.org/10.1029/2002JD002741, 2003.

843   Portafaix, T., Godin-Beekmann, S., Payen, G., de Mazière, M., Langerock, B., Fernandez, S., Posny, F., Cammas,
844   J.-P., Metzger, J.-M., Bencherif, H., Vigouroux, C., and Marquestaut, N.: Ozone profiles obtained by DIAL
845   technique at Maïdo Observatory in La Reunion Island: comparisons with ECC ozone-sondes, ground-based FTIR
846   spectrometer and microwave radiometer measurements, in: ILRC 27, 27th International Laser Radar Conference,
847   New-York, United States, 2015.

848   Raut, J.-C. and Chazette, P.: Retrieval of aerosol complex refractive index from a synergy between lidar,
849   sunphotometer and in situ measurements during LISAIR experiment, Atmospheric Chem. Phys., 7, 2797–2815,
850   https://doi.org/10.5194/acp-7-2797-2007, 2007.

851   Reichardt, J., Baumgart, R., and McGee, T. J.: Three-signal method for accurate measurements of depolarization
852   ratio with lidar, Appl. Opt., 42, 4909, https://doi.org/10.1364/AO.42.004909, 2003.

853   Rocadenbosch, F., Md. Reba, M. N., Sicard, M., and Comerón, A.: Practical analytical backscatter error bars for
854   elastic one-component lidar inversion algorithm, Appl. Opt., 49, 3380, https://doi.org/10.1364/AO.49.003380,
855   2010.

856   Sicard, M., Comerón, A., Rocadenbosch, F., Rodríguez, A., and Muñoz, C.: Quasi-analytical determination of
857   noise-induced error limits in lidar retrieval of aerosol backscatter coefficient by the elastic, two-component
858   algorithm, Appl. Opt., 48, 176, https://doi.org/10.1364/AO.48.000176, 2009.

859   Sicard, M., Baron, A. A., Ranaivombola, M., Gantois, D., Millet, T., Sellitto, P., Begue, N., Bencherif, H., Payen,
860   G., Marquestaut, N., and Duflot, V.: Radiative impact of the Hunga Tonga-Hunga Ha'apai stratospheric volcanic
861   plume: role   of   aerosols   and   water   vapor   in   the   southern   tropical   Indian   Ocean,
862   Preprints, https://doi.org/10.22541/essoar.170231679.99186200/v1, 2023.

863   Tidiga, M., Berthet, G., Jégou, F., Kloss, C., Bègue, N., Vernier, J.-P., Renard, J.-B., Bossolasco, A., Clarisse, L.,
864   Taha, G., Portafaix, T., Deshler, T., Wienhold, F. G., Godin-Beekmann, S., Payen, G., Metzger, J.-M., Duflot, V.,
865   and Marquestaut, N.: Variability of the Aerosol Content in the Tropical Lower Stratosphere from 2013 to 2019:
866   Evidence of Volcanic Eruption Impacts, Atmosphere, 13, 250, https://doi.org/10.3390/atmos13020250, 2022.

867   Vérèmes, H., Payen, G., Keckhut, P., Duflot, V., Baray, J.-L., Cammas, J.-P., Evan, S., Posny, F., Körner, S., and
868   Bosser, P.: Validation of the Water Vapor Profiles of the Raman Lidar at the Maïdo Observatory (Reunion Island)
869   Calibrated   with   Global   Navigation   Satellite   System   Integrated   Water   Vapor,   Atmosphere,   10,   713,
870   https://doi.org/10.3390/atmos10110713, 2019.

871

a supprimé: Sicard, M., Baron, A. A., Ranaivombola, M., Gantois, D., Millet, T., Sellitto, P., Begue, N., Payen, G., Marquestaut, N., and Duflot, V.: Radiative impact of the Hunga Tonga-Hunga Ha'apai stratospheric volcanic plume: role of aerosols and water vapor in the southern tropical Indian Ocean, Preprints, https://doi.org/10.22541/essoar.170231679.99186200/v1, 2023.

Code de champ modifié